J. Fluid Mech. (1992), *vol.* 236, *pp.* 127–165
Printed in Great Britain

The dynamics of intrusions into a thermohaline stratification

By S. GEOFFREY SCHLADOW†, ELLEN THOMAS AND JEFFREY R. KOSEFF

Environmental Fluid Mechanics Laboratory, Department of Civil Engineering, Stanford University, Stanford CA 94305-4020, USA

(Received 30 April 1990 and in revised form 19 August 1991)

Physical and numerical experiments were performed for a linearly stratified heat–salt system, uniformly heated at one endwall. The initial stratification was in the diffusive sense. Intrusions formed at the heated endwall and propagated out into the interior fluid. Three classes of flow were identified, based upon the gravitational stability ratio, R_ρ, and a lateral stability parameter, R_1. For $R_1 > 1$, a vertical lengthscale for the initial intrusion thickness was developed which agreed well with that observed in the physical experiments. In all cases, a region of salt fingering developed due to gradient reversal at the heated endwall. Two very distinct merging processes were observed depending on the specific flow class. The first process occurred under conditions of high gravitational and lateral stability, and appeared to be controlled by horizontal motions induced by the intrusions. The second process was observed under less stable conditions and was a result of vertical motions at the heated endwall within the intrusions themselves. In the least stable class of flow (low gravitational and lateral stability), the intrusions were found to be self-perpetuating in the sense that they continued to propagate following removal of the endwall heat flux.

1. Introduction

Double-diffusive convection typically occurs in vertically stratified thermohaline systems, where large differences in the diffusivities of temperature and salinity (NaCl) can lead to convective instabilities in what were initially gravitationally stable, diffusing systems. When the stabilizing gradient is provided by the component of lower diffusivity (salinity), the ensuing convection is termed the 'diffusive' mode. When the opposite is true, it is referred to as the 'finger' mode. In this paper we consider initial stratifications that conform to the 'diffusive' mode. When horizontal gradients of the components exist, a far greater variety of motions have been observed. (See for example Turner 1985.) They generally, however, take the form of distinct intrusions propagating away from the region of maximum horizontal gradient. Examples of aqueous environments conducive to such phenomena include salt-gradient solar ponds, geothermal fields, lakes, estuaries, and the oceans. While the primary motivation for studying double-diffusive phenomena originated in oceanography, the implications of this work have also been recognized in a large number of widely disparate fields.

Most experiments have considered the case of a vertical salinity gradient subject

† Presently at Centre for Water Research, Department of Civil & Environmental Engineering, University of Western Australia, Nedlands 6009, Australia.

to lateral heating. Chen, Briggs & Wirtz (1971) applied a constant temperature difference to a continuously stratified salt solution. Convection cells first formed along the heated wall. As time progressed these lengthened and formed layers separated by thin interfaces containing sharp temperature and salinity gradients. For small values of time the thickness of the convecting layers was found to approach the lengthscale,

$$h_r = (\alpha \Delta T_H)/(\beta \, dS/dy)_i, \tag{1}$$

where ΔT_H is the imposed horizontal temperature difference, $(dS/dy)_i$ is the initial vertical salinity gradient and $\alpha = -(1/\rho)\partial\rho/\partial T$ and $\beta = (1/\rho)\partial\rho/\partial S$ are the coefficients of thermal and saline expansion, respectively. This lengthscale corresponds to the height of rise of a fluid element in the stratified surroundings. A horizontal Rayleigh number based on this scale was defined as

$$Ra_H = (g\alpha \Delta T_H \, h_r^3)/(\nu \kappa_T), \tag{2}$$

and a critical value for Ra_H of 15000 ± 2500 was determined for the onset of instability. Here κ_T is the thermal diffusivity and ν is the kinematic viscosity. In considering a wider range of Rayleigh number, Huppert & Turner (1980) observed that the initial thickness decreased from h_r as Ra_H was increased above the critical value, but asymptotes to $0.6h_r$ for $Ra_H > 2 \times 10^5$.

When the heating is provided by a constant lateral heat flux, on the other hand, a critical value of the dimensionless heat flux parameter

$$R_I' = (-\alpha(q/k))/(\beta \, dS/dy)_i \tag{3}$$

was found to determine the onset of instability (Narusawa & Suzukawa 1981). Here q is the lateral heat flux per unit area, and k is the thermal conductivity of the fluid. When NaCl was used as the solute, cellular convection only occurred at values of $R_I' > 0.28$, even when the criterion of equation (2) was exceeded. Suzukawa & Narusawa (1982) investigated the structure of the convective layers for these same conditions. In contrast to the observations of Chen *et al.* (1971), they found that the small roll cells that formed along the heated wall quickly merged before forming outwardly propagating intrusions. In most other respects the intrusions were quite similar. The propagation speed of the intrusion fronts was found to be constant with time, and increased with increasing values of R_I'. By assuming that the horizontal and vertical lengthscales were identical at initiation Narusawa & Suzukawa (1981) proposed a vertical lengthscale,

$$h_{NS} \sim [(\nu \kappa_T)/(g\alpha(q/k))]^{\frac{1}{4}}, \tag{4}$$

applicable at the onset of convection, prior to any merging events. This lengthscale is independent of the stratification and predicts the same scale for all flows with identical heat flux.

Tanny & Tsinober (1988) partially reconciled the differences between the observations for constant-temperature and constant-flux boundary conditions. When approaching a constant temperature difference slowly (a condition more like a constant lateral heat flux), their data suggested a greater dependence on the ambient stratification and a weak, if any, dependence on the temperature difference in setting the thickness of the initial layers. The initial layers thus formed were found to be considerably thinner than suggested by the height of rise criterion (based on the temperature difference that the boundary was approaching), but subsequent merging produced the same final thickness. An empirical layer thickness, based on the results of Chen *et al.* (1971) for conditions close to the critical Rayleigh number, was shown

to agree with their observations. This thickness, based on the height of rise at the critical temperature difference, is given by

$$h_{\mathrm{cr}} = 9.2(\nu\kappa_T/(g(\beta\,\mathrm{d}S/\mathrm{d}y)_1))^{\frac{1}{4}}. \tag{5}$$

Unlike the scale proposed by Narusawa & Suzukawa (1981), it is a function of the ambient stratification not the applied heating. Furthermore, since (5) was derived empirically, it conveys little information on the dynamics of the intrusion initiation process.

The primary mechanisms of merging observed by Tanny & Tsinober were described (after Linden 1976) as 'interface breakdown' and 'interface migration' although no detailed measurements were provided to confirm the exact nature of the merging processes. What measurements there were, however, suggested that the densities across an interface just prior to merging were not identical. This prompted the speculation that the kinetic energy of vortices embedded within the intrusions may play a role in the merging process.

While the instabilities produced in all the above side heating experiments are double diffusive, they are at all times driven by the conditions at the boundary. It was shown qualitatively by Turner & Chen (1974), however, that it is possible for an instability formed at the boundary of an initially (gravitationally) stable two-component stratification to continue propagating even after the lateral heat flux is removed. This phenomenon was observed after impulsively applying temperature differences in the range 1–3 °C to the lateral boundary of a linearly stratified sugar/salt system. They speculated that this was due to the instability effectively tapping the potential energy of the unstable salt stratification. Rather than driving the process, the conditions at the boundary only provide a trigger for subsequent events.

Jeeveraj & Imberger (1991) considered a double-diffusive stratification, but with lateral heating provided by a constant wall temperature. Their failure to observe self-propagation of intrusions suggested that the flow parameters encompassed by the experiments were outside those for which such motions exist.

In related studies (Turner & Chen 1974; Chen 1975; Chen, Paliwal & Wong 1976; Linden & Weber 1977) the effects of introducing sloping boundaries into double-diffusively stratified systems have been investigated. The unstable boundary flows that ensue produce horizontal solute gradients and in time the flow turns outwards to form a series of equally spaced layers. Turner & Chen (1974) observed that there was a local reversal of gradients behind each advancing front which produced motions from the 'finger' regime, even though the original distributions were in the 'diffusive' sense. The sloping boundary appeared to provide just the initial destabilization (as in the side heated case). The subsequent propagation of the layers was observed to be self-perpetuating and unaffected by the boundary.

In summary, we note that while previous studies of the effects of lateral gradients have provided useful insight into the behaviour of these flows, most work has focused on the onset of instability, the thickness of the intrusions produced, and a qualitative description of the motions within the intrusions. With the exception of Turner & Chen (1974) and Jeeveraj & Imberger (1991), these studies have also been limited to singly stratified systems.

We focus in particular on four related issues. These are: (*i*) *What is the proper scaling for the initial layer thickness as a function of both heat flux and ambient stratification?* (*ii*) *How does the internal structure of the intrusions vary as a function of*

initial stratification and endwall heating rates? (iii) What are the primary mechanisms governing merging? (iv) Under what conditions are the intrusions self-propagating?

The approach taken is primarily experimental, but with the experiments being both physical and numerical. In the following section, a formal definition of the system is presented, from which scaled quantities for the intrusions can be deduced. The experimental apparatus, for both the laboratory experiments and the numerical experiments, is then described together with a description of the analytical techniques used. The results and the subsequent discussion specifically address the issues identified above.

2. Theoretical considerations

2.1. *System description*

The system we consider comprises negative, linear gradients of both temperature and species in the vertical, as shown schematically in figure 1. The working fluid is water, and the species gradient is provided by common salt (NaCl). The net density gradient in the vertical is such that the system is initially gravitationally stable. Vertical fluxes of temperature and salinity at the top and bottom boundaries are assumed to maintain the linear gradients. Initially the system is quiescent. At time $t = 0$, a constant heat flux is applied at the boundary defined by $x = 0$, and at some time thereafter intrusions begin developing at that boundary.

To simplify the equations, density is decomposed into the standard form such that $\rho = \rho_0 + \rho_e + \rho'$, where ρ is the total ambient density, ρ_0 is a reference density, ρ_e is the initial equilibrium density in the absence of motion, and ρ' is the density variation from equilibrium due to motion and diffusion. Furthermore, invoking the Boussinesq approximation yields the conservation equations (in two dimensions) for mass, momentum, energy, and species (Turner 1973):

$$\partial u/\partial x + \partial v/\partial y = 0, \tag{6}$$

$$\partial u/\partial t + u\,\partial u/\partial x + v\,\partial u/\partial y = -(1/\rho_0)\,\partial p'/\partial x + \nu\nabla^2 u, \tag{7}$$

$$\partial v/\partial t + u\,\partial v/\partial x + v\,\partial v/\partial y = -(1/\rho_0)\,\partial \rho'/\partial y - (\rho'/\rho_0)\,g + \nu\nabla^2 v, \tag{8}$$

$$\partial T'/\partial t + u\,\partial T'/\partial x + v\,\partial (T_e + T')/\partial y = \kappa_T \nabla^2 T' \tag{9}$$

and

$$\partial S'/\partial t + u\,\partial S'/\partial x + v\,\partial (S_e + S')/\partial y = \kappa_S \nabla^2 S'. \tag{10}$$

In (8) and (9) it has been assumed that the initial gradients are linear ($\partial S_e/\partial y =$ constant and $\partial T_e/\partial y =$ constant).

To classify the experiments, we use two dimensionless quantities, the Rayleigh ratio, R_ρ, and the lateral ratio, R_1. R_ρ is formed from the vertical saline and thermal Rayleigh numbers, given by $Ra_S = g\beta(\partial S/\partial y)\,h^4/\nu\kappa_T$ and $Ra_T = g\alpha(\partial T/\partial y)\,h^4/\nu\kappa_T$ (where h is an appropriate vertical lengthscale) and is defined as

$$R_\rho = (\beta\,\partial S/\partial y)/(\alpha\,\partial T/\partial y). \tag{11}$$

R_1, which is defined as

$$R_1 = -(\alpha(q/k))/(-\alpha\,\partial T/\partial y + \beta\,\partial S/\partial y)_i, \tag{12}$$

is a simple modification of that proposed by Narusawa & Suzukawa (1981), and explicitly takes into account the two-component vertical stratification. Physically it may be interpreted as the ratio between the density gradient at the heated boundary to the initial, net vertical density gradient.

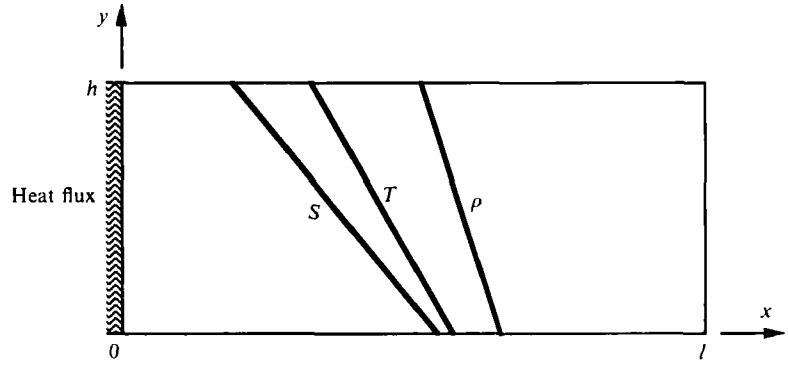

FIGURE 1. Schematic representation of flow system.

2.2. *Scaling*

Where lateral heating is achieved by applying a constant temperature difference, the height of rise of a fluid element subject to this temperature difference provides a natural vertical scale for these layers (Chen *et al.* 1971). If, however, only the boundary heat flux is specified, an estimate of the height of rise cannot be made independently of knowledge of the horizontal lengthscale.

In order to develop a more consistent scaling than that proposed by Narusawa & Suzukawa (1981) we consider the boundary region of the present system. First we make the usual boundary-layer assumptions that the velocity and lengthscales normal to the dominant flow direction (u and δ) are much smaller than those in the direction of flow (v and h). Next, at time $t = 0$ a constant heat flux, q, is applied, and heat is conducted to a thermal boundary layer with thickness $O(\delta_T)$ given by

$$\delta_T \sim \kappa_T^{\frac{1}{2}} t^{\frac{1}{2}}. \tag{13}$$

Initially buoyancy acts to accelerate the fluid contained within the boundary layer. Comparing the unsteady and viscous terms of the vertical momentum equation gives the ratio of these two terms to be $O(Pr^{-1})$, where $Pr = \nu/\kappa_T$, suggesting that at this stage the correct balance is between buoyancy and viscosity. The buoyancy term may be expressed as

$$g' = (\rho'/\rho_0)\, g = (-\alpha T' + \beta S')\, g, \tag{14}$$

where

$$T' \sim -vt(\partial T_e/\partial y) + (q/k)\,\delta_T, \quad S' \sim -vt(\partial S_e/\partial y). \tag{15a, b}$$

Note that T' is affected by horizontal diffusion as well as vertical advection up the wall, whereas the equilibrium salinity distribution is modified by vertical advection only. Substituting (15) into (14), we obtain

$$g' = -N^2 \Delta y + \alpha g (q/k)\, \delta_T, \tag{16}$$

where Δy is the vertical displacement at a time t after initiation of heating, and N is the buoyancy frequency defined such that $N^2 = -(g/\rho_0)(\partial\rho/\partial y)$.

The rising fluid will eventually reach a maximum height, h, and stop. (All our experimental results suggest that there is a hiatus between the initial rise up the wall and the onset of instability leading to lateral intrusions.) At this point $g' = 0$ and $\Delta y = h$ which gives

$$N^2 h = \alpha g (q/k)\, \delta_T \quad \text{or} \quad h/\delta_T \sim R_1. \tag{17}$$

Using the second term on the right-hand side of (16) as a scale for g', and applying the viscous–buoyancy balance yields

$$v \sim \alpha(q/k)\, gPr^{-1}\kappa_T^{\frac{1}{2}} t^{\frac{3}{2}} \tag{18}$$

and

$$\Delta y \sim \alpha(q/k)\, gPr^{-1}\kappa_T^{\frac{1}{2}} t^{\frac{5}{2}}. \tag{19}$$

Combining (17) and (19) gives

$$t_t \sim N^{-1} Pr^{\frac{1}{2}} \tag{20}$$

for the time at which Δy reaches the final height of rise h.

The vertical lengthscale h may then be calculated by combining (19) and (20) to obtain

$$h \sim R_1 N^{-\frac{1}{2}} \kappa_T^{\frac{1}{2}} Pr^{\frac{1}{4}}. \tag{21}$$

It should be noted that the boundary-layer analogy we are employing requires that $\delta_T < h$, and therefore the above analysis is only applicable for cases where $R_1 > 1$. The correct force balance for the case of $R_1 \sim 1$ is not apparent at this time.

3. Experimental considerations

3.1. *Physical experiments – apparatus*

The experimental facility consists of a 4.0 m long, 0.8 m wide and 0.5 m deep tank as shown in figure 2. The walls are of composite construction, the inner pane being 6.25 mm thick glass separated by a 6.25 mm air gap from an outer Plexiglas pane of similar thickness. Additional external insulation is provided by 25 mm, high-density styrofoam sheeting.

Opposing linear gradients of salinity and temperature are obtained by following the standard 'double bucket' method described by Oster (1965). Our experiences suggest that the inflow rate to the experimental facility be kept below 8 l min^{-1} to produce a smooth initial profile. In addition the experimental facility was preheated to about the mean stratification temperature to minimize heat loss and to circumvent 'ghost layers' being produced in a narrow boundary region at the walls. These are detectable by shadowgraphs projected through the width of the tank, but are not indicative of the uniform stratification away from the walls. Typical initial profiles are shown in figure 3.

As we have no way of imparting constant heat and salinity fluxes at the top and bottom boundaries to maintain the initial gradient, we have opted to deliberately include unstratified layers there. The depth of these layers is sufficiently large that transport of heat and salt down the gradient will only produce small temperature and salinity changes at the top and bottom, thereby approximating a constant flux condition for the duration of the experiment.

A constant heat flux for the lateral boundary is produced by radiant heating. As the initial water temperature varies linearly with vertical position, a constant wall temperature would have produced a similarly varying lateral heat flux. A set of four 250 W lamps and two translucent plastic light diffusers are housed in a reflective enclosure, which abuts the exterior endwall of the test facility as shown in figure 2. The multiple reflections within the enclosure together with the diffusers act to produce a uniform field of diffuse light which passes through both the glass and Plexiglas of the test section and is absorbed by a black film attached to the inside surface of the wall. At present a maximum flux of approximately 300 W m^{-2} is produced at the inside surface of the wall.

To calibrate the heat flux system, 30 cm of the tank closest to the heated wall was

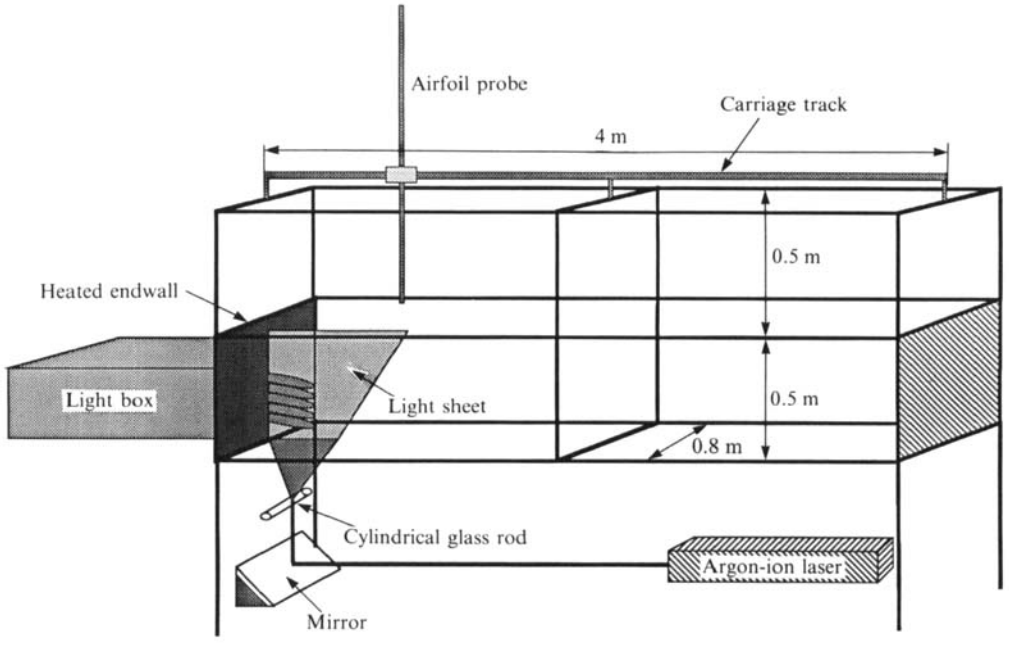

FIGURE 2. Schematic of experimental facility.

partitioned off from the rest of the facility and insulated on the bottom, sides and top. The section was filled with water and, with the heating lamps on, the water was vigorously stirred while the temperature at the centre was continuously recorded with a platinum resistance thermometer. The power drawn by the lamps at different rheostat settings was also recorded using a wattmeter. For all power outputs the water temperature was observed to rise linearly after an initial transient. This transient varied from approximately 30 to 180 s. The efficiency of energy transfer from the lamps to the water (as heat) was less than 2%, prompting us to conduct all experiments at the maximum lamp output.

Fast-response thermistor and conductivity probes are used to obtain vertical temperature and salinity profiles. The instruments used are Thermometrics FP07 thermistors and Precision Measurement Engineering 4-electrode conductivity sensors. Both instruments have spatial resolutions of less than 1 mm. The thermistors are calibrated using a platinum resistance thermometer, and have been found to be stable over many months. The conductivity sensors are less stable and are calibrated with a Seabird SBE4-01 conductivity sensor prior to every experiment. A thermistor/conductivity probe pair is driven vertically by a small DC motor at approximately 10 cm s^{-1}. Vertical position is determined using a linear potentiometer and the output of each probe and the potentiometer is sampled by computer at 100 Hz. The assembly is carriage mounted and may be manually positioned along the centreline (x-direction) of the facility. Depthwise profiles of salinity and density are computed from the acquired temperature and conductivity data. Expressions for calculating salinity and density are given by Head (1983) and Ruddick & Shirtcliffe (1979) respectively. The raw conductivity and temperature data is low-pass filtered at 30 Hz prior to computing the salinity.

Considerable use is made of video recording the flows, as a means of both reviewing experiments at a later time and for measuring whole field velocities. For the latter

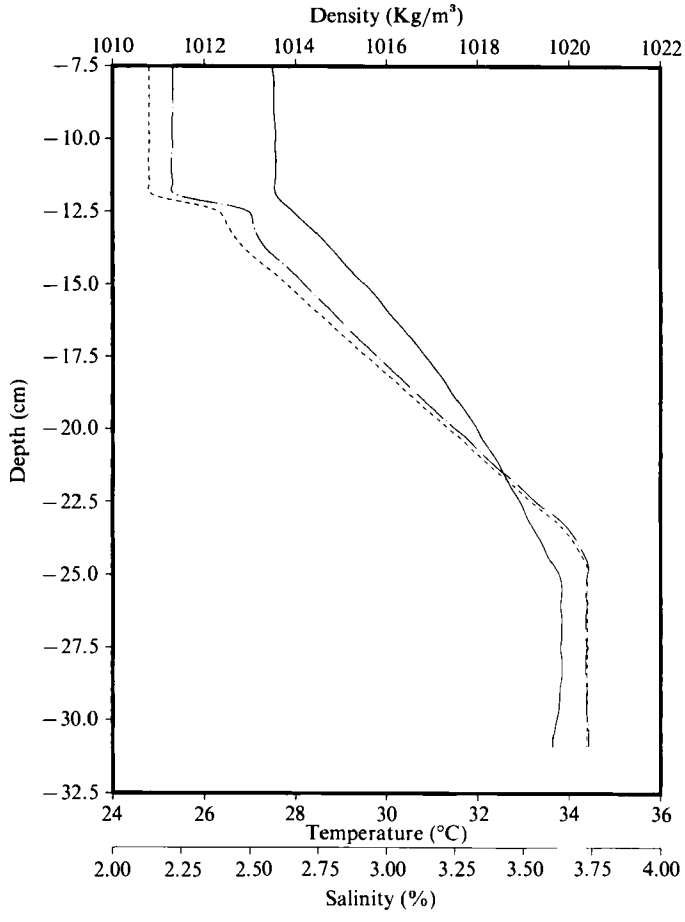

FIGURE 3. Typical initial T (——), S (– – –), and ρ (— · — ·) profiles, taken 13 mm from the heated endwall prior to initiation of heating for experiment I-5.

purpose the two storage tanks are seeded with tracer particles prior to filling the experimental facility. In this way a uniform particle density is assured. Pliolite VT resin, in the size range of 50–75 μm (S.G. of 1.03), added at a concentration of 0.0015 gm l^{-1}, has proved most satisfactory. In this size range and concentration particles stay suspended for over a week and are clearly visible when illuminated. For viewing the flows in a more qualitative sense, injections of small quantities of Rhodamine-B and Fluorescein dye (dissolved in water drawn from the centre of the gradient) have been used. Generally Fluorescein gives the most brilliant response in the argon-ion laser used for illumination. Rhodamine-B, however, with its weaker fluorescence allows the seed particles to remain visible, thus facilitating simultaneous flow visualization and particle tracking.

The light sheet is produced in a vertical plane normal to the endwall by passing a 1 W argon-ion laser beam through a glass rod and then directing the sheet through a thin slit in the external insulation at the bottom of the tank. This is shown schematically in figure 2. The camera views the experiment through a small port cut in the side insulation. Experiments are recorded at 30 frames per second by a monochrome CCD camera with 512 × 512 pixel resolution. The video signal is stored on a super VHS video recorder for subsequent digitization and processing.

Two-dimensional flow velocity fields have been generated by processing video images of the particle-seeded flow. By tracking consecutive images of the same particle for a known video framing rate, velocities can be determined throughout the plane of view, producing an array of two-dimensional velocity vectors. For the example shown in this paper (figure 22), in which the particle density was sufficiently high, streaks were generated over a time period of approximately 8 s. In some earlier experiments for which lower particle densities were used, several closely spaced 8 s realizations were combined to produce adequate resolution in the final velocity field. Only particles remaining in the laser light sheet throughout the entire 8 s time period are considered valid and may be used for subsequent determination of particle speed and direction of travel. Depthwise profiles such as those shown in figure 22 are produced by interpolating the field of velocity vectors onto a 20×20 grid using a spline technique (Rignot & Spedding 1988).

3.2. *Numerical techniques*

The numerical results were obtained using a variation of the SEAFLOS1 code (Perng & Street 1989). The code solves, in two dimensions, the finite-differenced forms of the unsteady mass, momentum, energy and species conservation equations on a spatially non-uniform grid. Though having its origins in the SIMPLE algorithm (Patankar 1980), SEAFLOS1 differs in some fundamental respects. These differences relate primarily to the use of quadratic upstream interpolation for the convective terms and a conjugate gradient scheme for the solution of an exact pressure equation. Time advancement is by an explicit, second-order predictor-corrector scheme. The equation solved by the code differ slightly from those given by equations (6)–(8). First, the Boussinesq assumption has not been invoked insofar as the effect of temperature and salt concentration on density and all other fluid properties has been explicitly retained. Second, the decomposition of density, temperature and salinity into reference, equilibrium, and perturbation quantities is not performed. Pressure is decomposed so as to remove the effect of the hydrostatic component. This code has previously been used to simulate time-varying, natural convection flows in cavities (Schladow, Patterson & Street 1989; Schladow 1990).

The necessity of solving the equations with spatial resolution sufficient to represent the interfaces between the intrusions makes direct simulation of the exact laboratory experiment impossible. Instead, we have chosen to simulate a physically smaller system, and focus at present on the initial layer formation. A 98×98 computational mesh is used to represent the 8 cm long and 2.91 cm high computational domain. In the vertical direction the mesh is uniform with the cell spacing being 3×10^{-4} m. A non-uniform mesh was used in the horizontal direction, based on the transform recommended by Roberts (1970). Close to the boundary, this produces a similar mesh size to the vertical mesh. Initially the domain is quiescent and continually stratified in salinity and temperature. The constant-heat-flux boundary condition at the left-hand vertical boundary is $q = 100 \pm 2.5$ W m^{-2}. The 'noise' in the flux is deliberately imparted using a random number generator so as to hasten the onset of the physical instability and therefore reduce computation time. The right-hand vertical boundary is adiabatic, and both vertical boundaries are non-conducting with respect to salinity and assumed to be no slip. The horizontal boundaries are free slip and have constant fluxes of both salinity and heat, with the flux values being those required to sustain the initial salinity and temperature gradients.

4. Results

4.1. *General*

Experiments were performed with the goal of obtaining a set of baseline data representative of the stability and dynamics of a two-component linearly stratified system subject to lateral heating. System stability is characterized by the two dimensionless parameters, R_ρ and R_l, defined by (11) and (12). Generally, a large value of R_l indicates strong lateral forcing and weak vertical stability, while a large value of R_ρ indicates weak double-diffusive effects and large gravitational stability. Experiments have been conducted over a wide range of parameter values in order to delineate the flow behaviour for a variety of stability conditions. Experimental parameters are summarized in table 2 (below).

The general evolution of the intrusions is common to all experiments. Initially small roll cells develop along the heated wall. In time these become more elongated and take the form of a series of fully or partially mixed layers separated by sharp density interfaces. At a later time they thicken by merging with neighbouring intrusions. Between each layer, strong shear is created along the interfaces by flow moving away from the wall in the upper region and back towards the wall in the lower region. The shear velocities are $O(1\ \mathrm{mm\ s^{-1}})$ whereas the propagation velocities of the intrusion fronts are an order of magnitude smaller. Motions near the endwall are also generally common to all experiments. A parcel of fluid very close to the endwall appears to rise until the salinity retained by that parcel inhibits any further upward motion. The parcel is then forced out away from the wall, cools, becomes denser than the surrounding fluid, and as a consequence tends to fall. This produces the characteristic downward slope of the intrusions adjacent to the wall. Eventually the fluid is entrained by the counterflow that comprises the bottom of each intrusion. This process continues as the initial convective cells combine to form larger intrusions.

4.2. *Stability classification*

The specific flow behaviour and structure of the intrusions vary significantly depending on the stability of the system. Three classes (I–III) of intrusion have been identified. The intrusions are distinguished by their characteristic dimension (h), propagation velocity (u_p), temperature (T) and salinity (S) fields, as well as their ability to continue propagating after the heat flux is removed. The characteristics of the intrusions are summarized in table 1.

Photographs and sample profiles for Classes I and II are shown in figures 4 and 5, respectively. The step-like nature of the profiles indicates the presence of the horizontal intrusions or convecting layers. For Class III, only sample profiles are shown, since the intrusions are very similar in appearance to those of Class II.

Class I flows, which seem to evolve under conditions of relatively high gravitational and lateral stability, are more quiescent than flows in Classes II and III. Overall the motions develop on a smaller scale and are characterized by lower velocities and less mixing. The convection cells develop into intrusions less than 10 mm in thickness which propagate slowly ($\sim$5–10 cm $\mathrm{h^{-1}}$) during the period of applied heat flux, but diffuse away when it is removed. They are therefore similar to the intrusions previously observed in single-component stratifications. As can be seen in figure 4(b), a relatively strong stable temperature stratification develops within the intrusions, accompanied by a well mixed or sometimes slightly unstable salinity distribution.

Motions in Class II are seemingly more dynamic than those in Class I. The intrusions propagate at a moderate speed ($\sim$10–30 cm $\mathrm{h^{-1}}$) away from the heated

Class	Final h (mm)	u_p (cm h^{-1})	T	S	Self-propagating?
I	<10	5–10	Stably stratified	Well-mixed	No
II	10–40	10–30	Stably stratified	Well-mixed	No
III	30–50	>25	Well-mixed	Well-mixed	Yes

TABLE 1. Summary of characteristics in the three flow classes

endwall, and develop into 10–40 mm thick layers. As in Class I, the intrusions stop propagating when the applied heat flux is removed, and the layered structure eventually diffuses back to a continuous stratification. Overall, much more active convection is observed visually in this class owing to the lower stability and stronger shear. Comparison of figures 4(*a*) and 5(*a*) confirms this point, and also suggests that vertical motions within the intrusions appear to be quite prevalent in Class II. The depthwise profiles in figure 5(*b*) indicate that within each intrusion the salinity is generally well mixed or slightly unstable, whereas the temperature develops a discernible stable stratification.

Motions in Class III are the most dynamic of the three classes, and occur under conditions of relatively low gravitational and lateral stability. Within the developed intrusions, mixing of both properties occurs relatively rapidly, yielding uniform profiles of temperature and salinity over layer depths of 30–50 mm, as shown in figure 6. The intrusions advance relatively quickly (>25 cm h^{-1}) and, although very similar in appearance, the motions in Class III are slightly more dynamic than those of Class II. As noted in table 1, however, the distinguishing characteristic of Class III flows is that the intrusions are *self-propagating*, that is, they continue to propagate out away from the endwall after the applied heat flux has been removed. This characteristic was also observed by Turner & Chen (1974).

4.3. *Scaling*

Table 2 shows the observed thickness (h_{obs}) of layers at initiation as given by the experimental and numerical data. The experiments with values shown for h_{obs} are only those for which dye was added to the fluid at commencement and the initial formation process was recorded on videotape. Experiments for which only vertical profiles were taken were unsuitable for this analysis as the distance from the wall to the closest profile was sufficient that layer merging may have already taken place. The thickness was calculated from the digitized video image and is an average of all layers which were marked by dye. Because of the degree of subjectivity involved in deciding what constitutes the edge of the layer at the boundary, the accuracy is within only ± 0.5 mm. For comparison to h_{obs}, table 2 also includes the vertical lengthscales h_{NS} (equation (4)), h_{cr} (equation (5)), and h (equation (21)). In addition, the time at which the thermal boundary layer first stabilizes (t_f) and its characteristic velocity (v) at that time are given. The value of infinity for R_ρ refers to the presence of a salt stratification only. The rows delineated by I-1 to III-2 refer to the physical experiments. (The Roman numerals I, II, and III refer to the three classes of flow described in the previous section.) The next row presents results from the numerical simulation, and the final rows (NS1-NS9) refer to the results of Narusawa & Suzukawa (1981).

Figure 7 compares measured intrusion thicknesses with the thickness scales

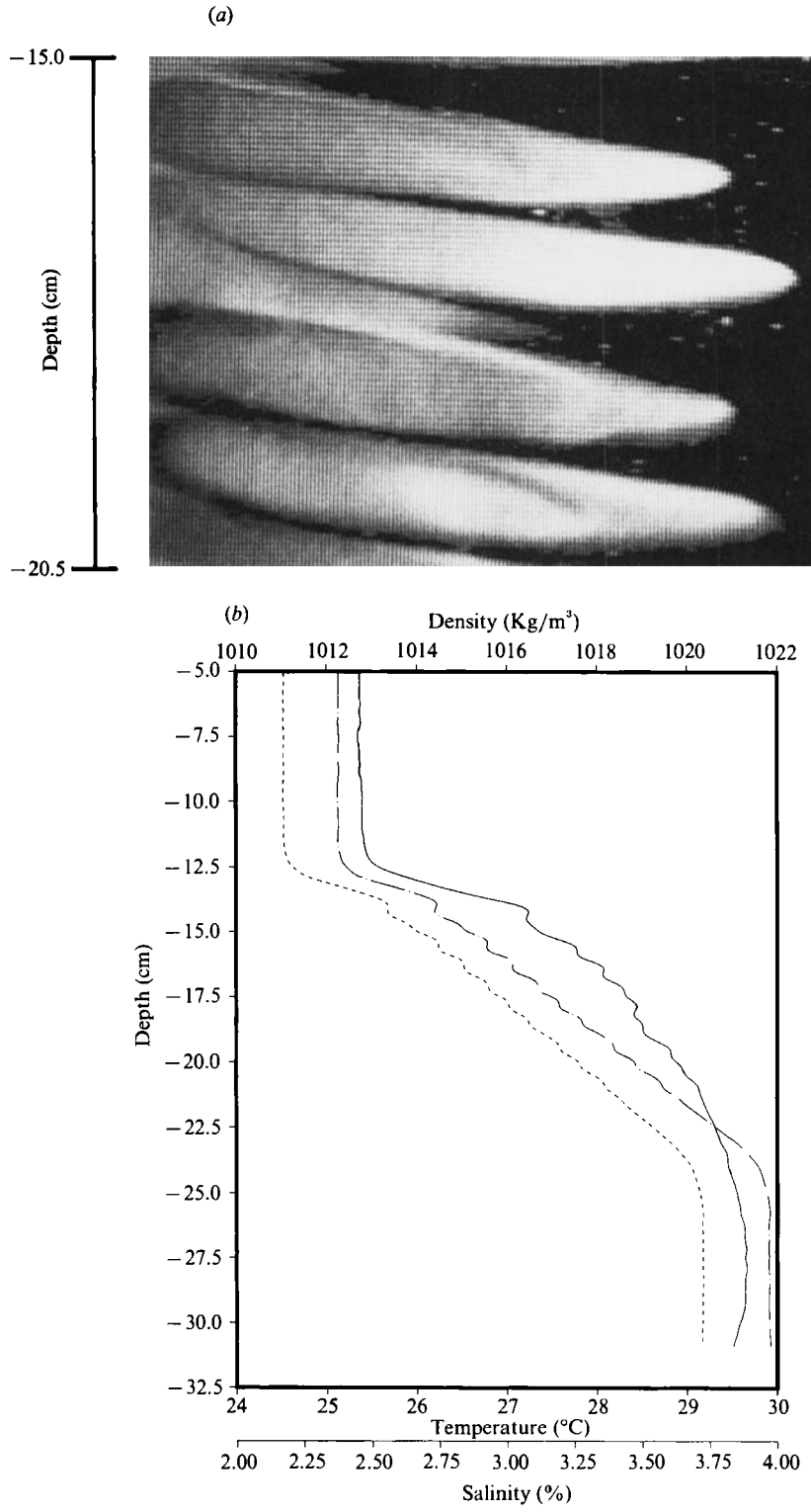

FIGURE 4. Class I (experiment I-4): (*a*) photograph taken at $t = 26$ min, (*b*) depthwise profiles of T (——), S (– – – –), and ρ (— · — · —) for $t = 26$ min. 13 mm from heated endwall.

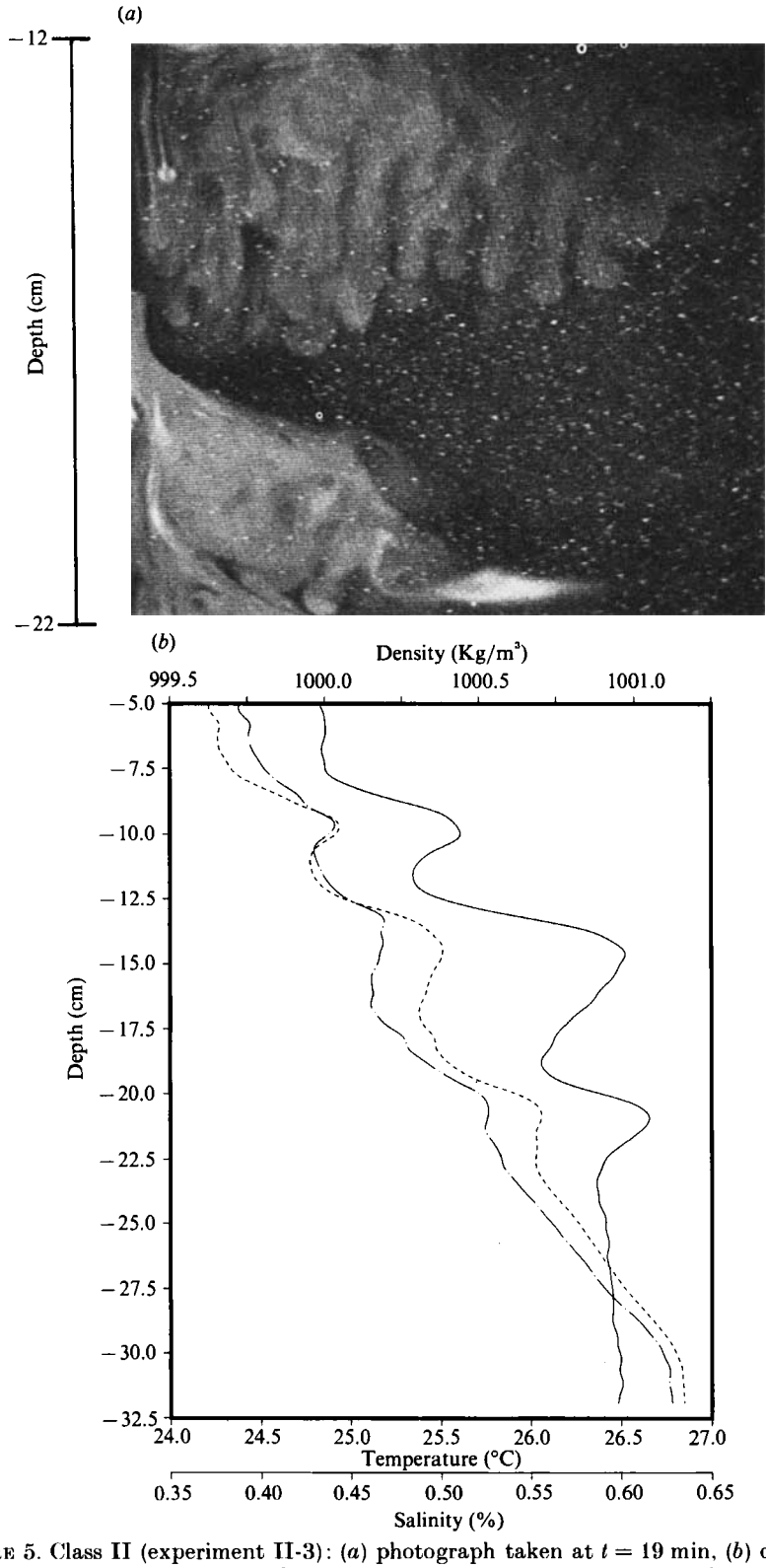

FIGURE 5. Class II (experiment II-3): (*a*) photograph taken at $t = 19$ min, (*b*) depthwise profiles of T (——), S (– – – –), and ρ (—·—·) for $t = 19$ min, 30 mm from heated endwall.

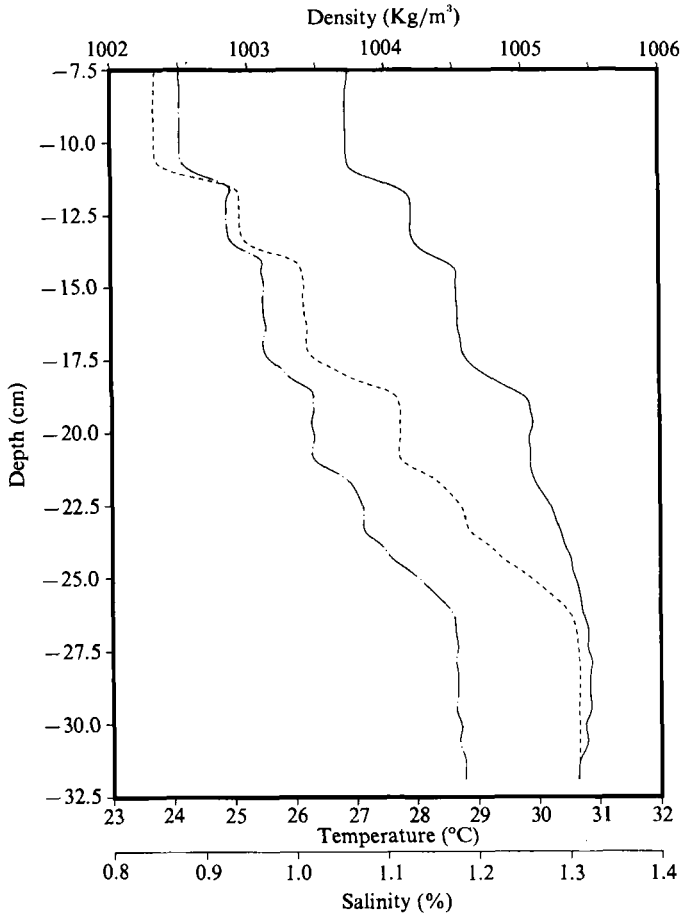

FIGURE 6. Class III (experiment III-2): depthwise profiles of T (——), S (– – – –), and ρ (—·—·) for $t = 51$ min, 50 mm from heated endwall.

described above. The values calculated for the vertical lengthscale h agree very well with the observed layer height for the experiments in which R_1 is sufficiently larger than one (Cases II-3, II-4, II-5, II-9, II-10, II-11, II-12, II-13), delineated by filled circles in figure 7. These experiments encompass the parameter range $2.2 < R_\rho < 9.1$ and $5.2 < R_1 < 12.9$. For all these cases the scale length is also in reasonable agreement with h_{cr}, the 'critical height' of Tanny & Tsinober (1988), although their scale tends to consistently overestimate the observed thickness. The lengthscale of Narusawa & Suzukawa (1981), h_{NS}, is constant for the same heat flux and shows no agreement with the data. Values of h and h_{cr} calculated for the experiments of Narusawa & Suzukawa (1981) (NS6-NS9 in table 2) both significantly underpredict their observed layer thickness, h_{obs}. This discrepancy is attributed to the fact that their observations were based on final layer thicknesses, measured from shadowgraph images following merging of the initial layers.

The form of equation (21) suggests that h_{obs} may be appropriately non-dimensionalized by $\kappa_T^{\frac{1}{2}} N^{-\frac{1}{2}} R_1$, assuming a constant Prandtl number. (Kelley 1984 has in fact suggested that $\kappa_T^{\frac{1}{2}} N^{-\frac{1}{2}}$ is an intrinsic layer thickness scale for oceanic thermohaline staircases.) The resulting dimensionless lengthscale, h^*, is plotted versus R_1 in figure 8. For high values of $R_1 (> 5)$, h^* is approximately constant,

Case	q (W m^{-2})	$\left(\frac{\partial T}{\partial y}\right)_i$ (°C m^{-1})	$\left(\frac{\partial s}{\partial y}\right)_i$ (‰ m^{-1})	R_ρ	R_1	h_{obs} (mm)	h_{NS} (mm)	h_{cr} (mm)	h (mm)	t_f (s)	δ_T (mm)	v (mm s^{-1})
I-1	100	0	4.39	∞	1.4	6	0.7	13.3	1.1	4.8	0.8	0.24
I-2	100	13.53	5.71	9.8	1.4	—	0.7	12.5	1.1	4.5	0.8	0.25
I-3	100	14.34	5.33	9.3	1.4	—	0.7	12.7	1.1	4.6	0.8	0.24
I-4	100	25.37	10.33	8.3	0.9	6	0.7	10.8	0.6	3.4	0.7	0.18
I-5	100	40.65	10.17	5.1	1.0	5	0.7	10.9	0.7	3.5	0.7	0.20
I-6	100	23.95	9.95	9.7	0.8	6	0.7	10.9	0.6	3.4	0.7	0.16
II-1	100	3.75	0.59	4.2	13.9	—	0.7	22.1	20.2	15.1	1.5	1.34
II-2	100	5.37	0.78	3.9	10.7	—	0.7	20.6	14.6	13.3	1.4	1.10
II-3	100	7.01	0.84	3.2	10.8	18	0.7	20.3	14.8	13.3	1.4	1.11
II-4	100	12.02	1.51	2.9	7.3	12	0.7	17.5	8.7	10.2	1.2	0.85
II-5	100	20.03	2.49	2.6	5.2	8	0.7	15.5	5.6	8.2	1.1	0.68
II-6	100	11.32	1.18	2.6	9.2	—	0.7	18.6	11.9	11.9	1.3	1.0
II-7	100	28.94	3.94	2.6	3.6	—	0.7	13.8	3.4	6.5	1.0	0.53
II-8	100	14.25	1.31	2.3	9.0	—	0.7	18.1	11.5	11.7	1.3	0.98
II-9	100	14.25	1.32	2.3	9.0	13	0.7	18.1	11.5	11.7	1.3	0.98
II-10	100	21.70	2.21	2.2	6.4	7.4	0.7	15.9	7.3	9.3	1.1	0.79
II-11	300	4.79	1.87	9.1	12.9	13	0.5	16.6	13.5	7.8	1.0	0.57
II-12	200	21.70	2.05	2.2	12.8	15	0.6	16.2	14.8	9.6	1.2	0.77
II-13	200	21.84	2.28	2.4	10.9	14	0.6	15.8	12.1	8.8	1.1	0.69
III-1	100	15.15	1.38	2.1	10.0	—	0.7	17.9	12.9	11.9	1.3	1.08
III-2	100	14.43	1.40	2.1	10.5	—	0.7	17.8	13.5	11.9	1.3	1.14
Num	100	83.33	17.86	5.0	0.5	2	0.7	9.4	0.3	2.7	0.6	0.11
NS1	64	0	17.9	∞	0.19	—	0.91	9.4	0.11	2.4	0.6	0.07
NS2	107	0	32.0	∞	0.22	—	0.76	8.1	0.11	1.8	0.5	0.05
NS3	90	0	20.0	∞	0.28	—	0.79	9.1	0.16	2.2	0.6	0.07
NS4	160	0	42.2	∞	0.29	5.9	0.65	7.6	0.14	1.6	0.5	0.05
NS5	85	0	5.8	∞	0.60	10.8	0.92	12.4	0.46	4.1	0.8	0.12
NS6	464	0	14.1	∞	2.0	10.1	0.53	10.0	1.22	2.7	0.6	0.10
NS7	1070	0	13.2	∞	5.15	13.6	0.42	10.1	3.22	2.8	0.6	0.11
NS8	854	0	5.1	∞	9.81	31.5	0.45	12.9	7.71	4.4	0.8	0.20
NS9	1600	0	4.9	∞	20.0	68.0	0.38	13.0	16.0	4.6	0.8	0.21

TABLE 2. Results of scaling analysis. Experiments I-1 to III-2 refer to physical experiments in Classes I, II and III. Num refers to the numerical simulation. NS1–NS9 refer to the experiments of Narusawa & Suzukawa (1981).

suggesting that this scaling is indeed valid. Furthermore, the invariance in h^* for $R_1 > 5$ indicates that, although (21) is asymptotically valid for $R_1 \gg 1$, it may be applied to a fairly wide range of R_1 values (>5). For $R_1 < 5$, however, the scaling breaks down as $h \to \delta_T$, and the boundary-layer assumptions are no longer applicable. The h^* values calculated for the Narusawa & Suzukawa (1981) data show a similar trend. They are larger (note different scales in figure 8) owing to their measurement of h_{obs} following merging of the initial layers.

The values of the timescale, t_f, suggest that the setting of the vertical lengthscale occurs quickly, and considerably before lateral intrusions commence. Generally, the time between initiation of heating and commencement of roll cells was observed to be an order of magnitude larger than the boundary-layer timescale, t_f. Part of this time lag may be due to the transient period before the applied lateral heat flux becomes constant.

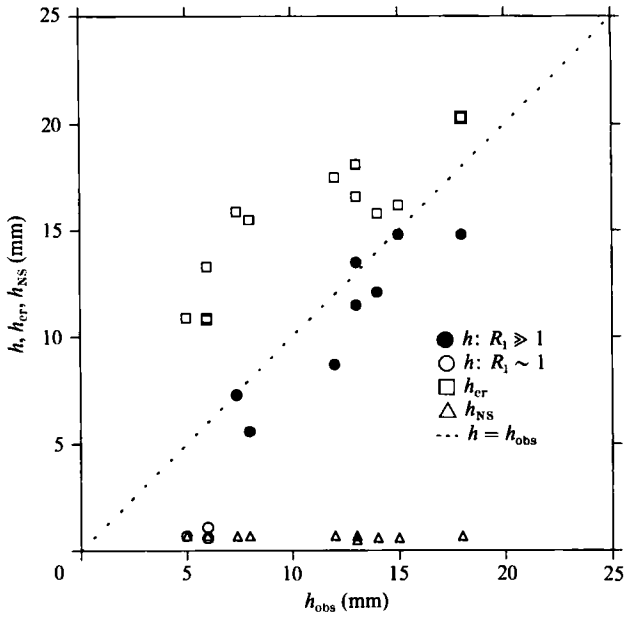

FIGURE 7. Three alternative intrusion-thickness scales as functions of the measured thickness, h_{obs}.

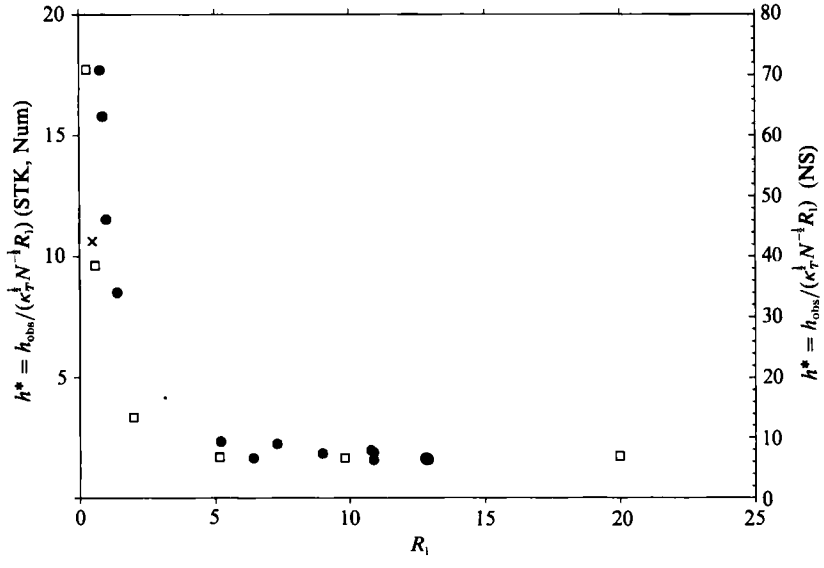

FIGURE 8. Non-dimensional vertical lengthscale, h^*, *vs.* R_l. Scaling (equation (21)) is only valid for $R_l \gg 1$. STK, present experiments (●); Num, numerical results (×); NS, Narusawa & Suzukawa.

4.4. *Numerical results*

The picture of the temporal evolution of the intrusion structure is augmented by the numerical simulation results. Owing to intense computing requirements for such simulations only one numerical case has been considered to date. This case has initial temperature and salinity gradients of 83.3 °C m^{-1} and 17.9% m^{-1} respectively, and

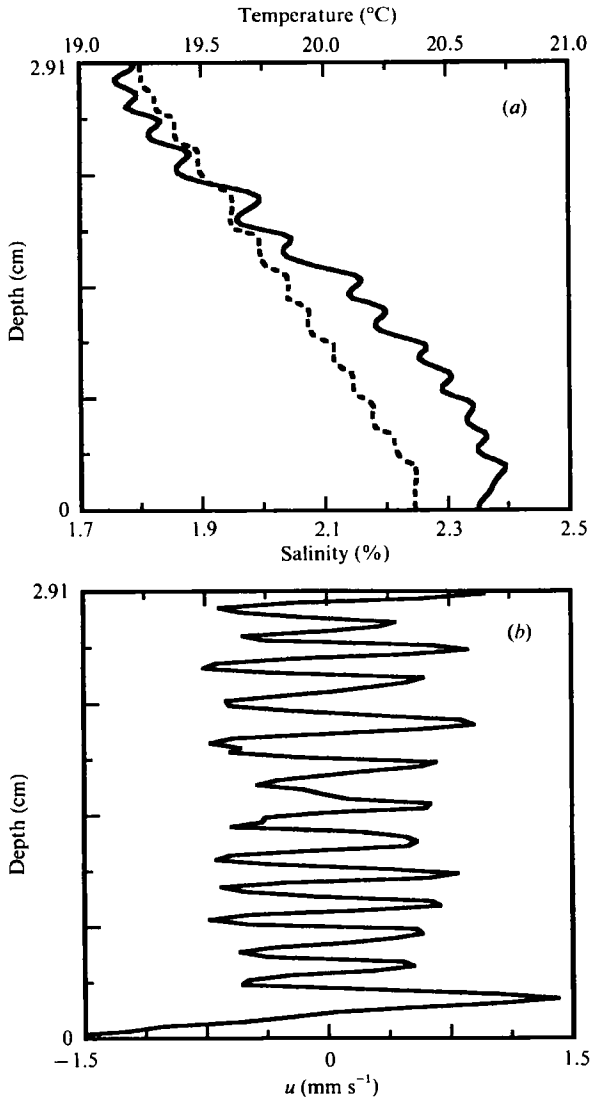

FIGURE 9. Vertical profiles from numerical simulation of Class I at $t = 3$ min and 1.5 mm from heated endwall: (*a*) temperature (——) and salinity (– – – –), (*b*) horizontal velocity.

an endwall heat flux of 100 W m^{-2}, producing a flow with $R_\rho = 5.0$ and $R_1 = 0.5$. It was chosen because it is realizable despite the very resource-intensive (5 s of CRAY X/MP time for every 0.0125 s computational timestep) demands of the computations. It is not, unfortunately, covered by the scaling analysis, and has proven difficult to realize experimentally with the present apparatus. However, despite this and the fact that the solution has not been advanced to the stage where merging would be expected, the results do conform with the experimental results in this general parameter range (Class I) and it is possible to make some observations regarding the early stages of layer formation. In what follows, horizontal sections of T, S, u and v will be presented along the $y/h = 0.5$ section. In these profiles $x/l = 0$ corresponds to the heated wall and $x/l = 0.4$ is a point 3.2 cm away from the wall.

Figure 9(*a*) shows profiles of temperature and salinity 180 s after commencement

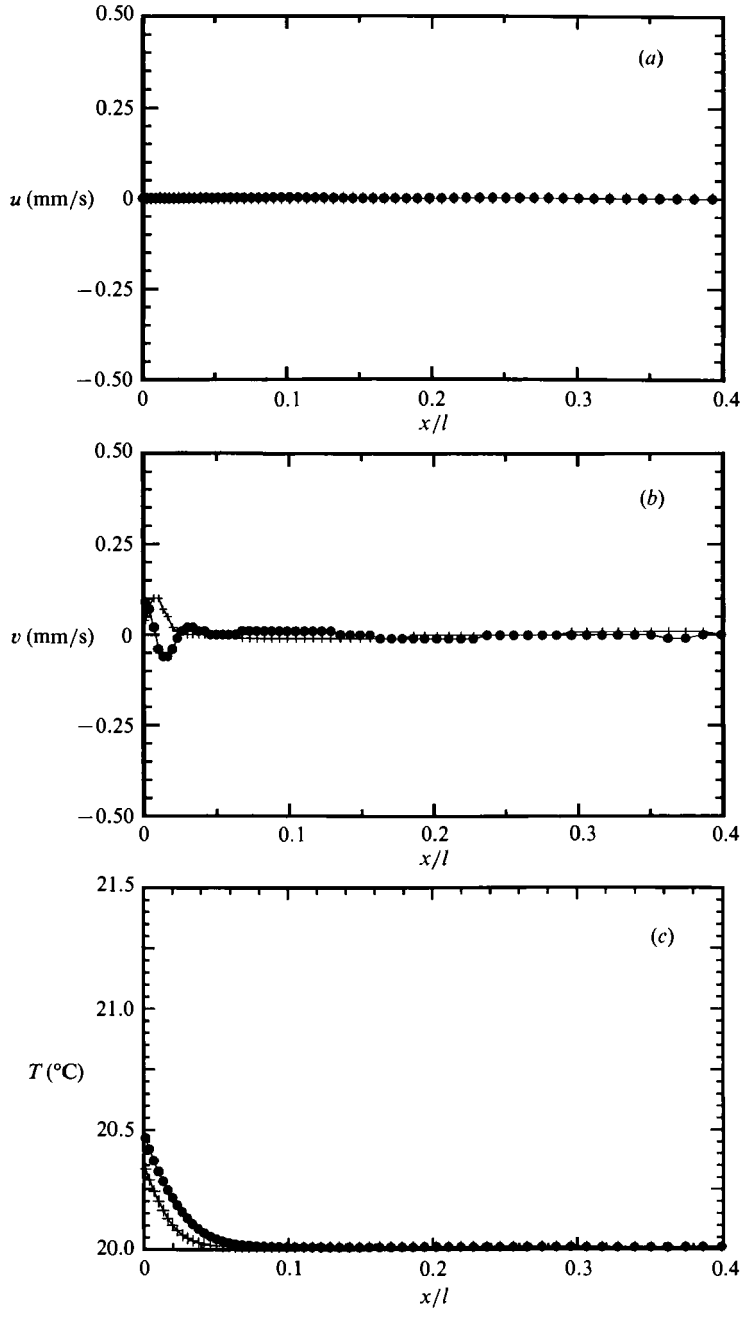

FIGURE 10(*a–c*). For caption see facing page.

of heating. The profiles are taken 1.5 mm ($x/l = 0.018$) from the endwall. The step-like structure of the intrusions is clearly evident. Note that, as in the experimental results for Class I, salinity is well mixed whereas a stable temperature gradient has been established within each intrusion. The profile of horizontal velocity at the same location and time is shown in figure 9(*b*). The numerical results differ from experiments for Class I in that the intrusions are much thinner and they develop far

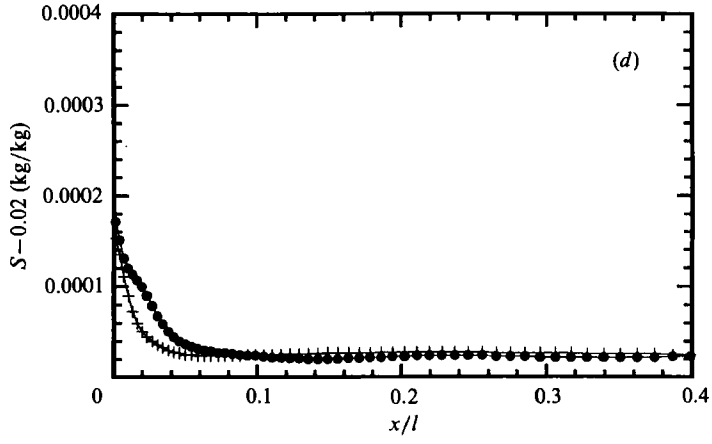

FIGURE 10. Horizontal profiles from numerical simulation of Class I at: +, $t = 10$ s; ●, $t = 20$ s. (*a*) Horizontal velocity, (*b*) vertical velocity, (*c*) temperature, (*d*) salinity.

sooner. This first difference can in part be accounted for by the values of R_ρ and R_1, while the latter difference may be due to the transient in the wall heating rate for the laboratory experiments. As will be seen, the detailed view of the formation of these intrusions presents a far more complex picture than figure 9 suggests. It also provides some indications of the dynamics of layer initiation in the case for which $R_1 < 1$.

Figure 10 shows sections at $t = 10$ and 20 s. After 10 s the temperature and salinity profiles are as one would expect for a side heated cavity. Thermal and saline boundary layers have formed and velocity is in the positive y-direction (up the wall). The magnitude of the velocity is relatively small (~ 0.1 mm s^{-1}), but is comparable to the scale velocities in table 2. Horizontal velocities are negligible in comparison. By $t = 20$ s, the flow reverses (see figure 10*b*): the fluid closest to the wall still moves upwards, but the adjacent fluid now moves downwards at about the same rate. This is the first apparent effect of the double-diffusive nature of the stratification. At this time, u is still negligible.

Figure 11 shows profiles at $t = 70$ and 80 s. The shape of the salinity profile is in contrast to the still quite regular shape of the temperature profile. It is suggestive of salt fingering (whether it is 'true' salt fingering or just convective instability driven by the salt distribution is not clear at this stage), with the regions of small positive slope being the fingers and the regions of large negative slope being the interfaces between rising and descending fingers. Given that the observed scale of these fingers is < 1 mm, the timescale for diffusion of heat across them would be ~ 10 s, producing the relatively smooth temperature field. On the other hand, salt, with effectively no diffusion, is retained, and drives the convective flow in the fingers. This picture is confirmed by the vertical velocity profile which shows the regions of flow reversal coinciding with the 'interfaces'. The velocities associated with this mechanism are significantly larger than those associated with the endwall heating flow at the earlier times. An interesting feature is also evident in the horizontal velocity field; within the boundary layer, velocities are negligible, while outside an oscillatory horizontal velocity develops. The period of these oscillations is $O(10$ s), which is comparable to the buoyancy period $T_N \sim 6$ s. The magnitude of the horizontal velocity is still much smaller than the vertical velocity.

This type of flow pattern appears to climax at $t = 90$–100 s after which the pattern

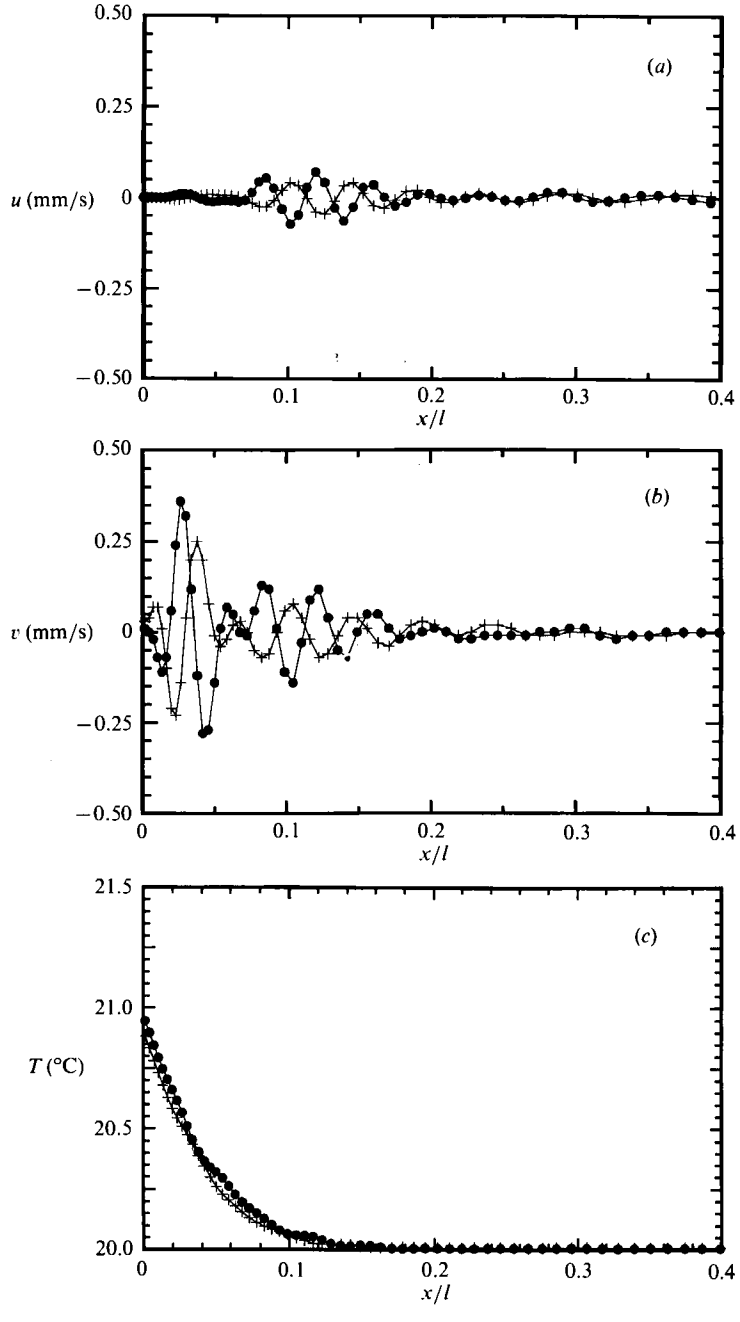

FIGURE 11 (*a–c*). For caption see facing page.

again changes. This corresponds to the time at which clearly formed intrusions are first observed in the flow. Clearly formed intrusions are identified as ones in which there is a degree of vertical mixing, typified by small circulation regions embedded within the intrusions.

Figure 12 shows profiles at $t = 150$ and 160 s. The salinity profile, though still not smooth, does not have the same clear step-like pattern evident earlier. The vertical

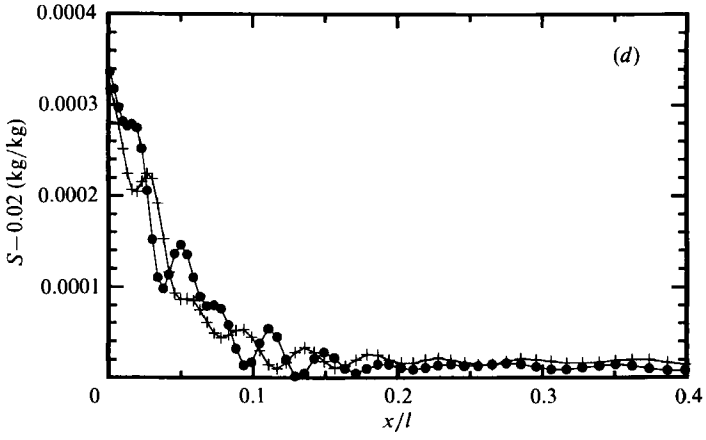

FIGURE 11. Horizontal profiles from numerical simulation of Class I at: +, $t = 70$ s; ●, $t = 80$ s. (*a*) Horizontal velocity, (*b*) vertical velocity, (*c*) temperature, (*d*) salinity.

velocity field is also far more complex now. Most significantly, the horizontal velocity in the boundary region ($x/l < 0.1$) is relatively large and, in fact, dominates the convection. The u-velocity at $x/l = 0.04$ is negative (motion towards the wall) while further out it is positive (motion away from the wall). This pattern appears because the intrusions tilt downwards and the section at $y/h = 0.5$ first passes through the bottom of one intrusion and then through the top of an underlying intrusion.

Figure 13 shows pathlines between $t = 160$ and 180 s. These were produced by releasing a field of tracer 'particles' at $t = 160$ s and then updating the particle positions every 1 s using the calculated velocity fields. The dots are the tracer positions at $t = 160$ s. This integrated view of the flow shows intrusions propagating away from the heated wall, dominated by large jet-like outflows along their upper boundaries, and similar inflows along their lower boundaries. The interfaces are therefore regions characterized by high shear. The cores of the intrusions are complex at this stage, with evidence of both recirculation zones and smaller scale oscillations. The oscillations referred to earlier away from the wall are also still evident here.

The reason the intrusions appear to form at the bottom first is due to the influence of the bottom boundary, as noted previously by Thorpe, Hutt & Soulsby (1969). As the flow commences, a flow towards the wall is produced at the bottom boundary in order to meet the entrainment demand. This flow can have two effects. First, the fluid moving up the wall near the bottom boundary is of the same density, as it is drawn from the same horizontal layer at the bottom. This is in contrast to the situation further up the wall, where the fluid is of progressively decreasing density. As a consequence, when the fluid that was originally at the base of the wall at time $t = 0$ reaches its height of rise and turns into the interior of the tank, the motion is followed by the fluid elements behind it. This depth defines the upper boundary of the intrusive layer. This layer than acts in a similar way for the fluid above it, and a second layer establishes itself, and so on. Such a mechanism was first described by Mendenhall & Mason (1923). The second effect is that the horizontal inflows could in fact perturb the vertical boundary layer and hasten the onset of double-diffusive instability at the bottom of the wall. This then influences the development of instability immediately above it and so on up the endwall.

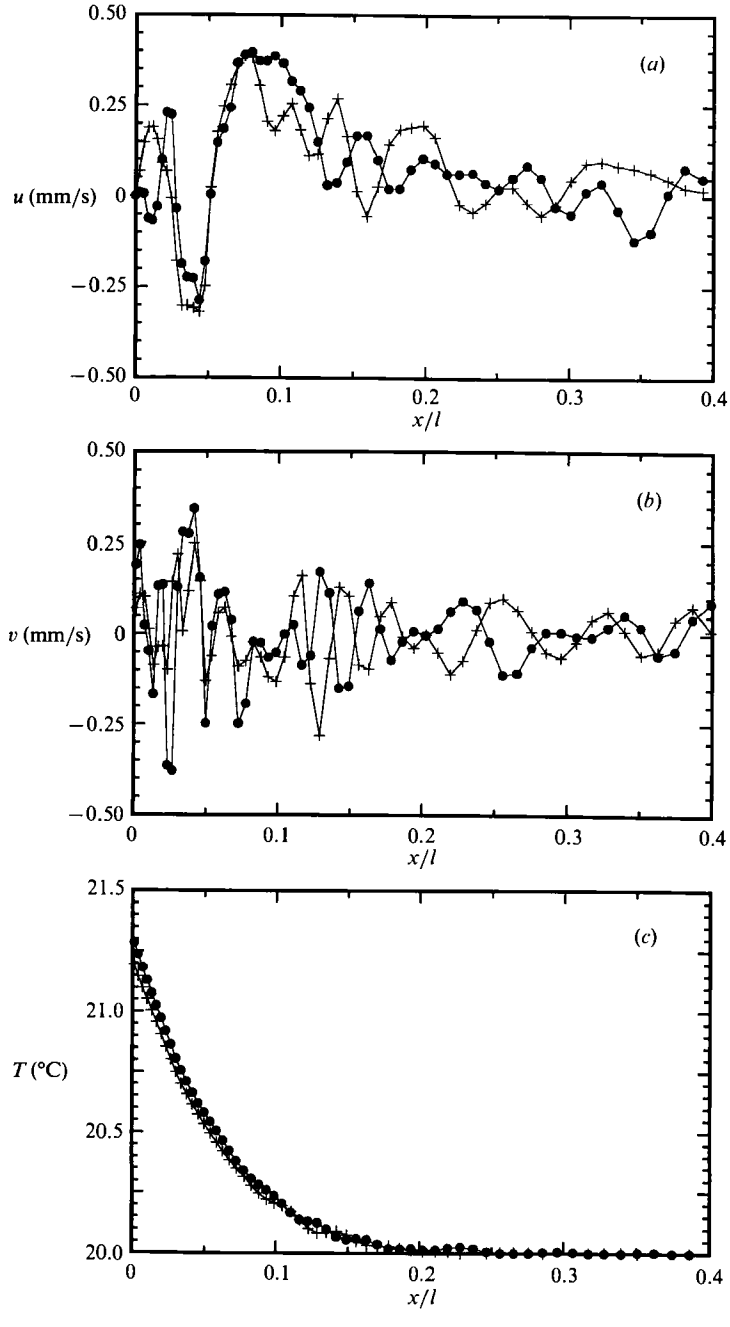

FIGURE 12(a–c). For caption see facing page.

5. Discussion

5.1. *Internal structure of intrusions*

Further insight into the physical processes governing the behaviour of the intrusions can be gained by examining plots of temperature versus salinity such as that shown in figure 14(a). (The interpretation to be presented here is similar to that of

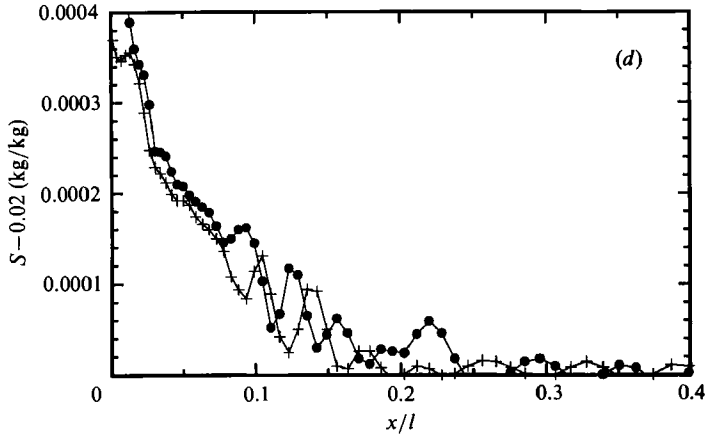

FIGURE 12. Horizontal profiles from numerical simulation of Class I at: +, $t = 150$ s; ●, $t = 160$ s. (*a*) Horizontal velocity, (*b*) vertical velocity, (*c*) temperature, (*d*) salinity.

Posmentier & Houghton 1978 for oceanic measurements.) The data shown are those used to produce the Class II profiles in figure 5(*b*). The endpoint in the lower left corner of the figure corresponds to a depth 5 cm below the water surface. Each cross marks an increase in depth of 1 cm.

To aid in interpreting the T–S diagram, figure 14(*b*) has been provided. This circle (plotted on the same axes as figure 14(*a*) to preserve the scales of temperature and salinity) may be used to match the slope at any point on the T–S curve to a particular point on the circle. The slope at any point on the circle corresponds to a particular stability condition. This can be gravitational stability (net density gradient is negative and both the salinity and temperature components have stable gradients); gravitational instability (net density gradient is positive); 'diffusive' (net density gradient is negative but only the salinity component provides the stability); or 'finger' (net density gradient is negative but only the temperature component provides the stability). The parameter R_ρ^* is the stability ratio for the 'finger' case and is defined as the inverse of R_ρ, that is $R_\rho^* = (\alpha\,\partial T/\partial y)/(\beta\,\partial S/\partial y)$. The circle is directional, with the arrows pointing towards increasing depths. The slope of the T–S curve at any point corresponds to a unique stability condition which can conveniently be determined by finding the point on the circle with the identical slope and proper directional sense. As an example, consider the regions denoted as interfaces in figure 14(*a*). Moving along the T–S curve in the direction of increasing depth (from lower left to upper right), the slopes are positive at all points. The region of the circle which corresponds to this signature is that labelled as 'diffusive' in the lower right quadrant. This is not surprising since the initial stratification was in the diffusive sense.

The loop-like structures between the interfaces are the convective layers. Approaching the loop labelled ABC from the bottom of the diagram (i.e. the top of the water column), we are in a 'diffusive' region. Closer to point A the slope becomes less steep, indicating that this region of the interface is very stable. At point A the slope moves into a gravitationally unstable region, proceeds into the 'finger' zone at point B, and finally at point C returns to the 'diffusive' condition. Point C represents the top of the next interface. Each of the other convective layers exhibits a similar pattern of travel from 'diffusive' to 'unstable' to 'finger' and finally back to 'diffusive'. The vertical structure of the layers is illustrated schematically in figure

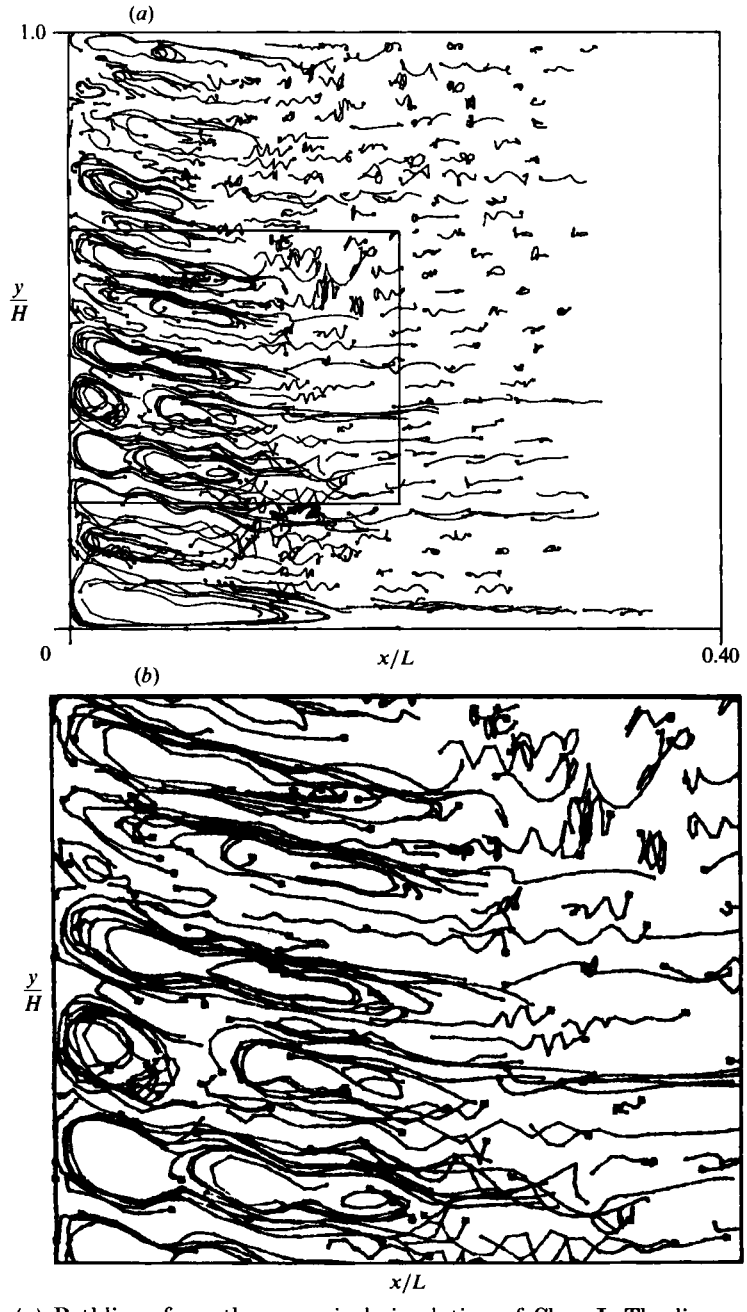

FIGURE 13. (*a*) Pathlines from the numerical simulation of Class I. The lines are produced by releasing a field of tracer 'particles' at $t = 160$ s and updating the positions every 1 s until $t = 180$ s, (*b*) enlargement of section indicated in (*a*).

15. As the probe travels down through an intrusion, it encounters a diffusive interface followed by a gravitationally unstable region and finally a fingering region before penetrating another diffusive interface overlying the next intrusion. This type of pattern is precisely what was observed from the flow visualization, although it was not possible to ascertain from the flow visualization alone whether the observed

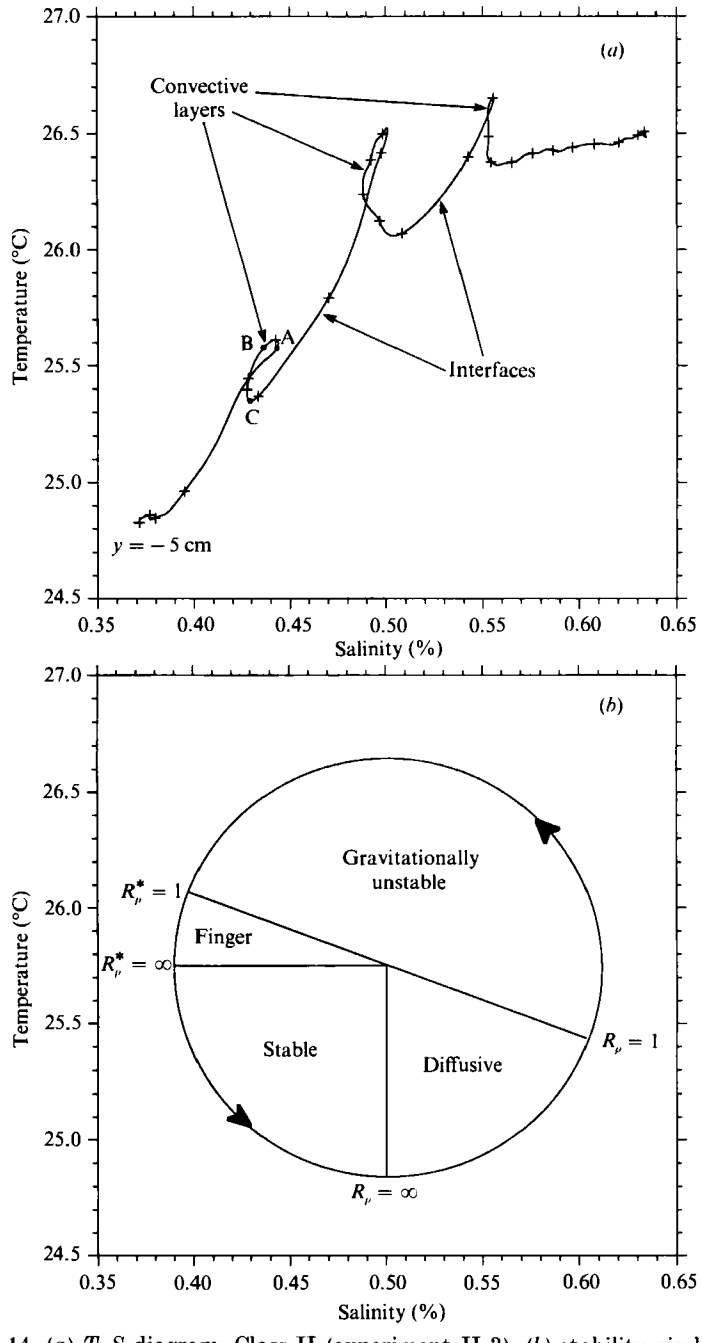

FIGURE 14. (*a*) *T*–*S* diagram, Class II (experiment II-3), (*b*) stability circle – see text for explanation.

'finger-like' structures were simple gravitational instabilities or salt fingers. These *T*–*S* plots suggest that they are indeed salt fingers, with just the upper part of the convecting layers being gravitationally unstable.

Figures 16(*a*) and 16(*b*) show an analogous set of diagrams for the Class I flow discussed earlier and represented by figure 4. The general pattern is similar to that

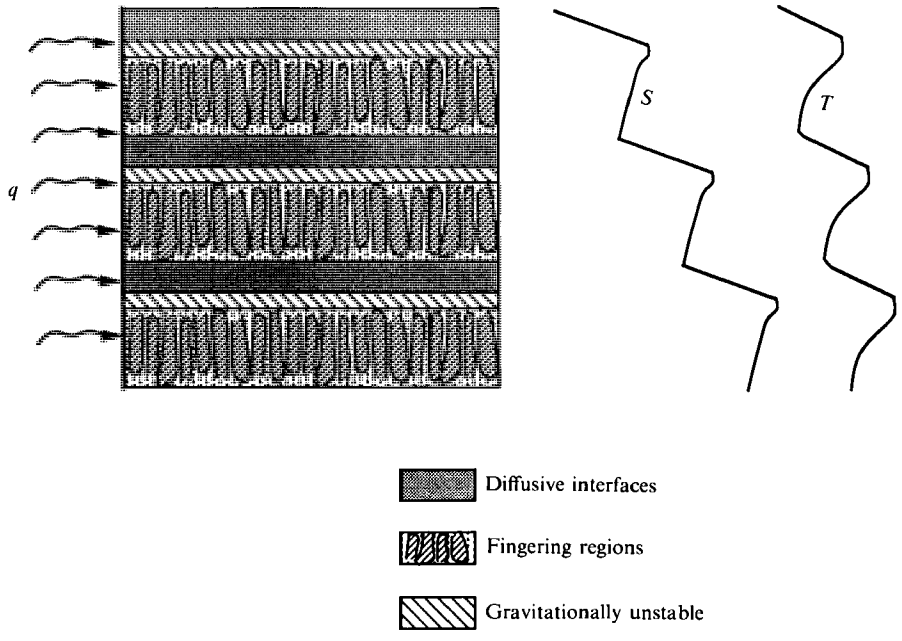

FIGURE 15. Schematic representation of vertical layer structure near the heated endwall.

of Class II except that the loop regions are much smaller in relation to the interfaces. (The interfaces and convective regions themselves are much smaller in Class I.) The presence of the loops indicates that salt fingering is even occurring in Class I, though it was not evident from the flow visualization.

The presence of fingering in Classes I and II provides an explanation for the vertical T and S profiles observed in each of these classes. As described earlier, vertical profiles in both classes are characterized by stabilizing temperature and slightly destabilizing or well-mixed salinity stratifications within the layers. Since fingering motions are known to transport salt much more efficiently than temperature, one would expect this type of vertical signature in the profiles. In Class III, while loops similar to those shown in figure 14 have also been observed, the fingering region is not as prevalent as in Class II. Both salinity and temperature tend to mix more quickly over the vertical extent of the layers owing to the stronger convective motions in this class.

Loop-like structures, similar to those in figures 14 (*a*) and 16 (*a*), are known to occur as a result of response time or spatial mismatch between a thermistor and conductivity probe (Osborn 1988). Indeed, experiments performed to estimate the error due to mismatch indicate that the magnitude of this error is of the same order as the salinity (and density) variations measured within the loops. However, independent confirmation of this description may be obtained from the T–S diagram of figure 17, produced from the numerical simulation data. As discussed earlier, the velocity profiles indicate that fingering-like motions are present in the flow. In order for fingering to occur, the correct property distributions must be present, and the loops in figure 17 provide us with evidence that this is indeed the case. Thus, it appears that salt fingering does indeed occur within the convecting layers in all classes.

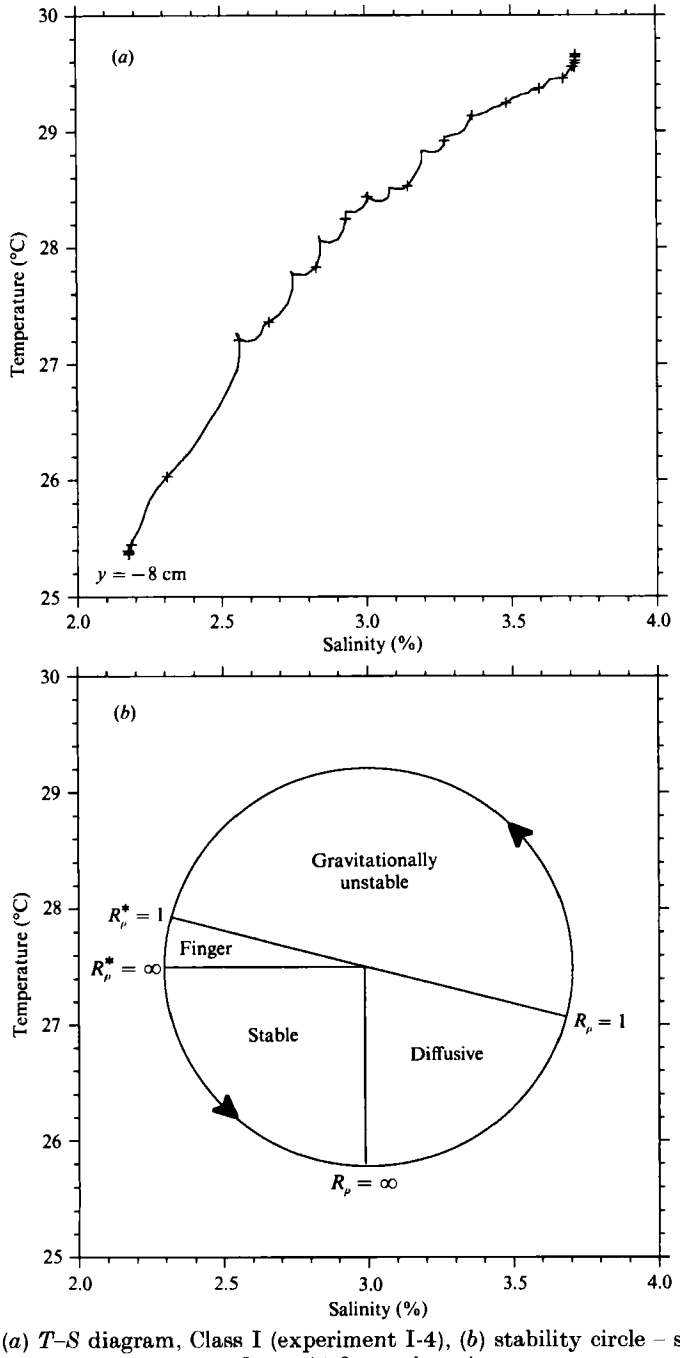

FIGURE 16. (*a*) *T*–*S* diagram, Class I (experiment I-4), (*b*) stability circle – see text describing figure 14 for explanation.

5.2. *Merging*

Two different merging processes have been observed in our experiments to date. The first applies to Class I and is governed primarily by horizontal motions and blocking effects. The second applies to Class II, and in contrast to Class I, is dominated by strong vertical fingering motions which penetrate adjacent layers.

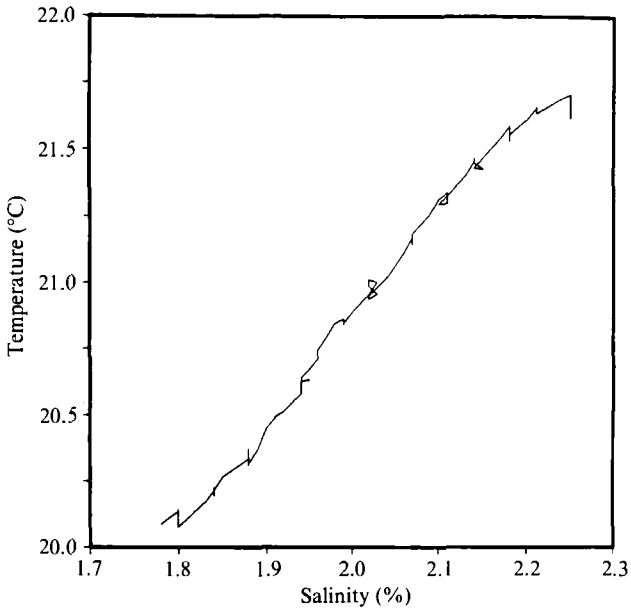

FIGURE 17. T–S diagram from numerical simulation of Class I.

A sequence of images showing Class I intrusions at successive times after initiation of heating is shown in figure 18. Initially R_ρ was 8.3 and R_1 was 0.9. Intrusions first appear after 10–15 min. At 24 min, the third intrusion from the top has begun to recede, and after 30 min has receded almost to the endwall where it becomes fully entrained by the adjacent overlying intrusion. After 41 min, the intrusion at the top of the region shown has merged with the intrusion above it, as has the partially shown intrusion at the bottom of the image. Thus the original set of seven intrusions has been reduced to four.

This sequence illustrates a case where the merging process is controlled by motions external to the intrusions themselves. It has been frequently observed that shear waves propagate ahead of the advancing intrusions. A vertical dye streak placed ahead of the intrusions would, for example, distort into a sinusoidal pattern reflecting the horizontal flows and counterflows of the intrusions. Flows ahead of the upper half of the intrusions move away from the wall, and are balanced by counterflows in the lower half. The middle intrusion of figure 18 (the first to merge) initially behaves in this way, but eventually the larger flow (and counterflow) of its neighbours literally overwhelms it, gradually forcing it back towards the wall. (A similar process has been observed by Maxworthy 1987 for a field of 'fingers' (not double diffusive) in a Hele-Shaw cell.)

A density profile taken at $t = 26$ min, 13 mm from the endwall is shown in figure 19. Note that the vertical extent of this profile corresponds directly to the 5.5 cm sections shown in figure 18. The interfaces between the original seven intrusions are still well defined, supporting the notion that merging is not caused by equalization of densities between the intrusions away from the endwall. Indeed, a detailed examination of the interfaces between intrusions of all classes showed that in virtually every case the interface value of R_ρ actually increased above the initial R_ρ, producing a more stable interface. Furthermore, our observations indicate that

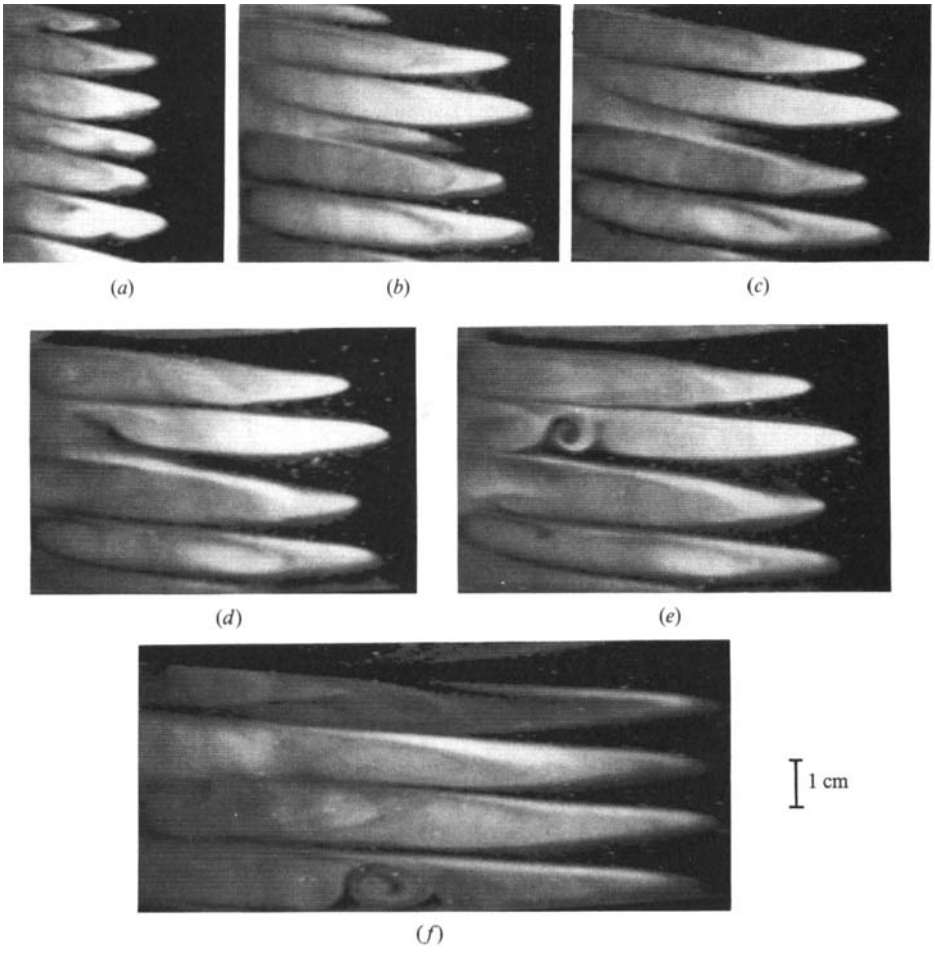

FIGURE 18. Merging sequence for experiment I-4: (*a*) $t = 17.5$ min, (*b*) $t = 24$ min, (*c*) $t = 26$ min, (*d*) $t = 28$ min, (*e*) $t = 30$ min, (*f*) $t = 41$ min.

merging appears to be initiated not at the endwall as suggested by Tanny & Tsinober (1988), but rather, at the intrusion fronts. Here, blocking causes particular intrusions to stop advancing. These intrusions are then entrained by their upper neighbours at the endwall, until they are completely engulfed.

The second type of merging process observed suggests that motions within the intrusions themselves may have a role in the merging process. A sequence of images for a Class II flow is shown in figure 20. Initial values of R_ρ and R_1 were 3.2 and 10.8 respectively. In this case, intrusions began to form ~ 1–2 min after initiation of heating. Although only one intrusion can be seen at early times in figure 20 owing to the absence of dye, intrusions are present throughout the entire depth of the image. At later times dye has been entrained from the lower intrusion, as well as the overlying mixed layer, so that motions could be visualized over the whole depth.

The initial formation takes place much more rapidly and is followed by a merging process dominated by strong vertical motions near the heated endwall. After 10 min the intrusion marked by dye in figure 20 is already beginning to merge with the intrusions above it. In contrast to Class I, the merging appears to be caused by

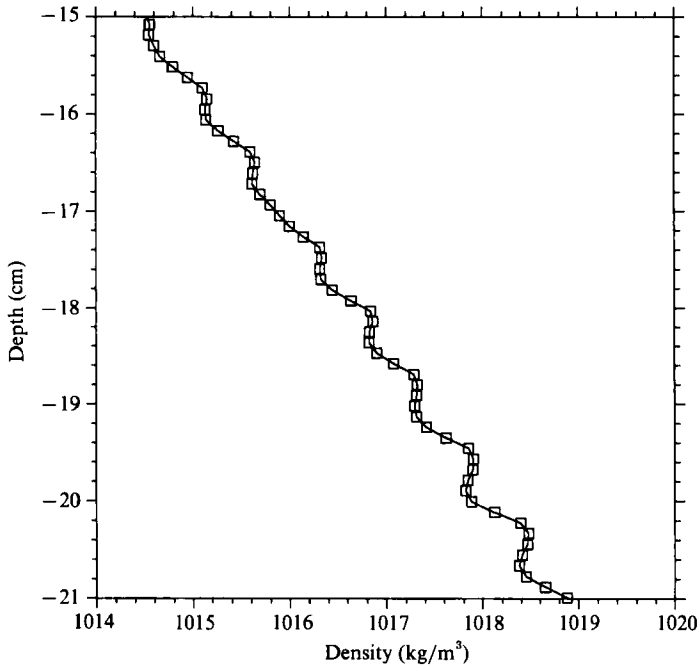

FIGURE 19. Density profile for experiment I-4 at $t = 26$ min, 13 mm from the heated endwall.

penetration of the vertical motions near the endwall into the adjacent layers. This penetration leads to interface breakdown, in the vicinity of the wall only, and subsequent merging of the adjacent layers. After about 20 min, the intrusions have reached their final thickness. By this time fingering motions are clearly visible in the upper layer due to the process described earlier in which warm, salty water is inserted above colder, fresher water as a result of the lateral heating.

Merging events have been observed to directly affect the propagation velocity (u_p) of intrusion fronts, as illustrated by the data in figure 21. The propagation velocities in this figure were computed by measuring the advance of a typical intrusion front over a known interval of time from video recordings of experiments. The actual intrusion front was delineated by the sharp interface between the dyed intrusion and the clear ambient fluid. As mergings of other intrusions were not occurring simultaneously and as only a fraction of the intrusions were in the camera's field of view, it was not possible to calculate an ensemble-average velocity. The figure is presented in dimensionless form, with $u^* = u_p/\kappa_T \delta_T^{-1}$ and $t^* = t_p/Lv^{-1}$. Here t_p is the time since the intrusion commenced propagating, L is the total length of the flume (4 m) and δ_T and v are the scale values at the time when $g' = 0$, shown in table 2.

Following the initial formation period, an intrusion moves relatively quickly from the wall. In time, it tends to slow down and may indeed approach a constant velocity as suggested by Narusawa & Suzukawa (1981). Results from experiment II-3 indicate, however, that this pattern is not necessarily followed in all cases. In this particular experiment, the intrusion slowed down significantly after about $t^* = 0.04$, continued moving relatively slowly until $t^* = 0.36$, at which time its speed of propagation substantially increased. Examination of the images in figure 20 sheds some light on the case of these variations. The images indicate that during the period

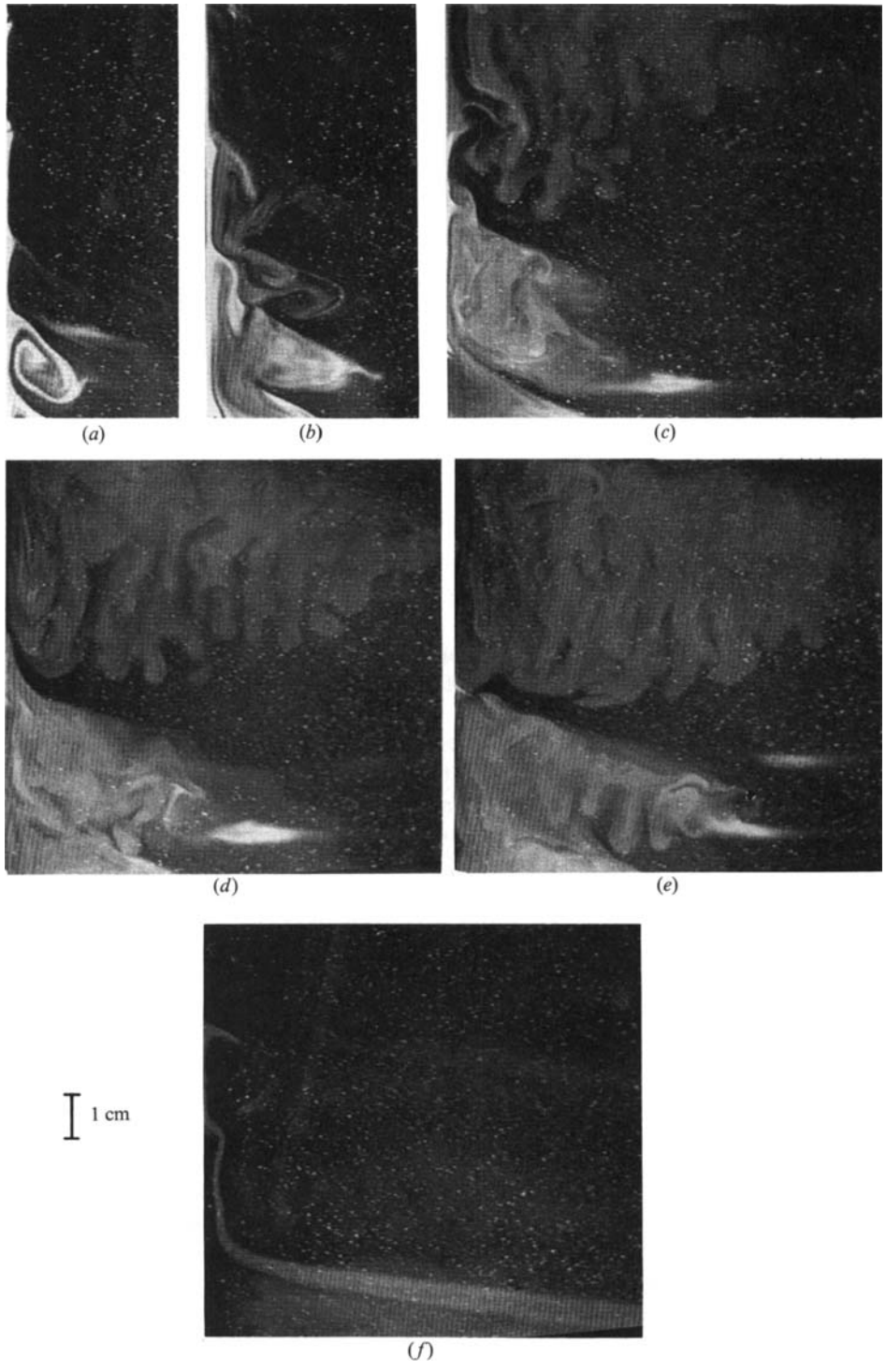

FIGURE 20. Merging sequence for experiment II-3: (*a*) $t = 3.5$ min, (*b*) $t = 9.5$ min, (*c*) $t = 17$ min, (*d*) $t = 20$ min, (*e*) $t = 22$ min, (*f*) $t = 51$ min.

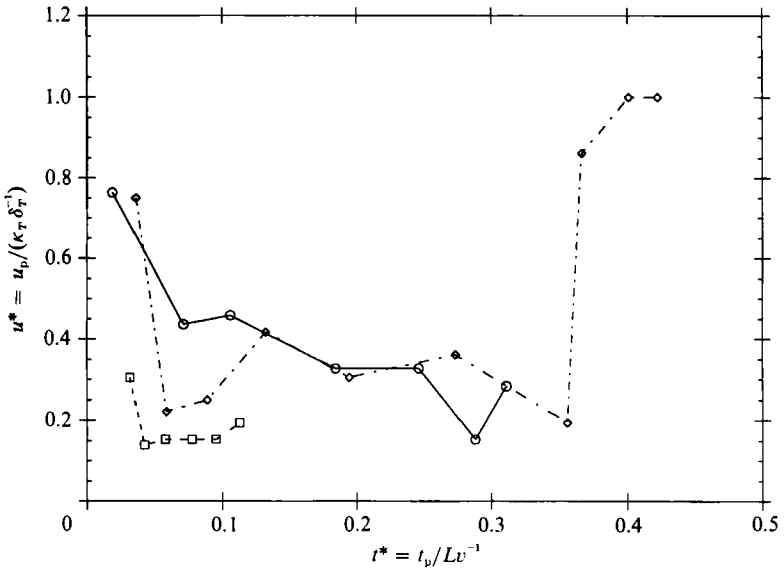

FIGURE 21. Dimensionless propagation velocity, u^*, *vs.* dimensionless time, t^* for particular intrusions in the experiments: —○—, II-5; --□--, I-4; —·◇·—, II-3.

of relatively slow propagation, the motions within the intrusions were dominated by fingering and were primarily in the vertical direction. During this time the initial convection cells were merging to form larger intrusions. Following the merging event, when the intrusions had reached their final thickness, the horizontal motions again became significant, thus increasing the speed of propagation. Large variabilities in propagation speed were observed in nearly all of the experiments and, as suggested by these results, may be closely associated with the merging process itself.

Shear instability appears to play little to no role in the two merging processes described. At the interfaces, strong horizontal motions are set up away from the wall at the top of each intrusion and back towards the wall at the bottom, creating regions of relatively high shear. Figure 22(*a*) shows a streak image taken over an 8 s time period 100 min after initiation of heating in the Class II experiment described above. The corresponding velocity vector plot and a vertical cross-section 5.8 cm from the endwall are shown in figures 22(*b*) and 22(*c*). Calculation of the Richardson number, $Ri = [g\,\partial\rho/\partial y]/[\rho(\partial u/\partial y)^2]$ across the intrusion interface yields values of $Ri \sim 3$–10, indicating that the interfaces are very stable.

5.3. *Self-propagation*

In an earlier section we described the behaviour of the intrusions after removal of the endwall heat flux. It was found that the Class I and II intrusions stopped growing and diffused away whereas once the destabilizing influence was removed, the Class III intrusions continued to propagate. Intrusions falling into this latter class typically correspond to the least-stable initial stratification conditions. Figure 23 shows profiles from experiment III-2 taken 3680 mm from the heated endwall (at the far end of the tank). The profiles in figure 23(*a*) were taken 93 min after initiation of heating. After 193 min, the heating was discontinued, and at this time the intrusion fronts had reached a distance of approximately $x = 2000$ mm from the endwall. At $t = 793$ min the profile in figure 23(*b*) was taken. As is clearly evident from the step-

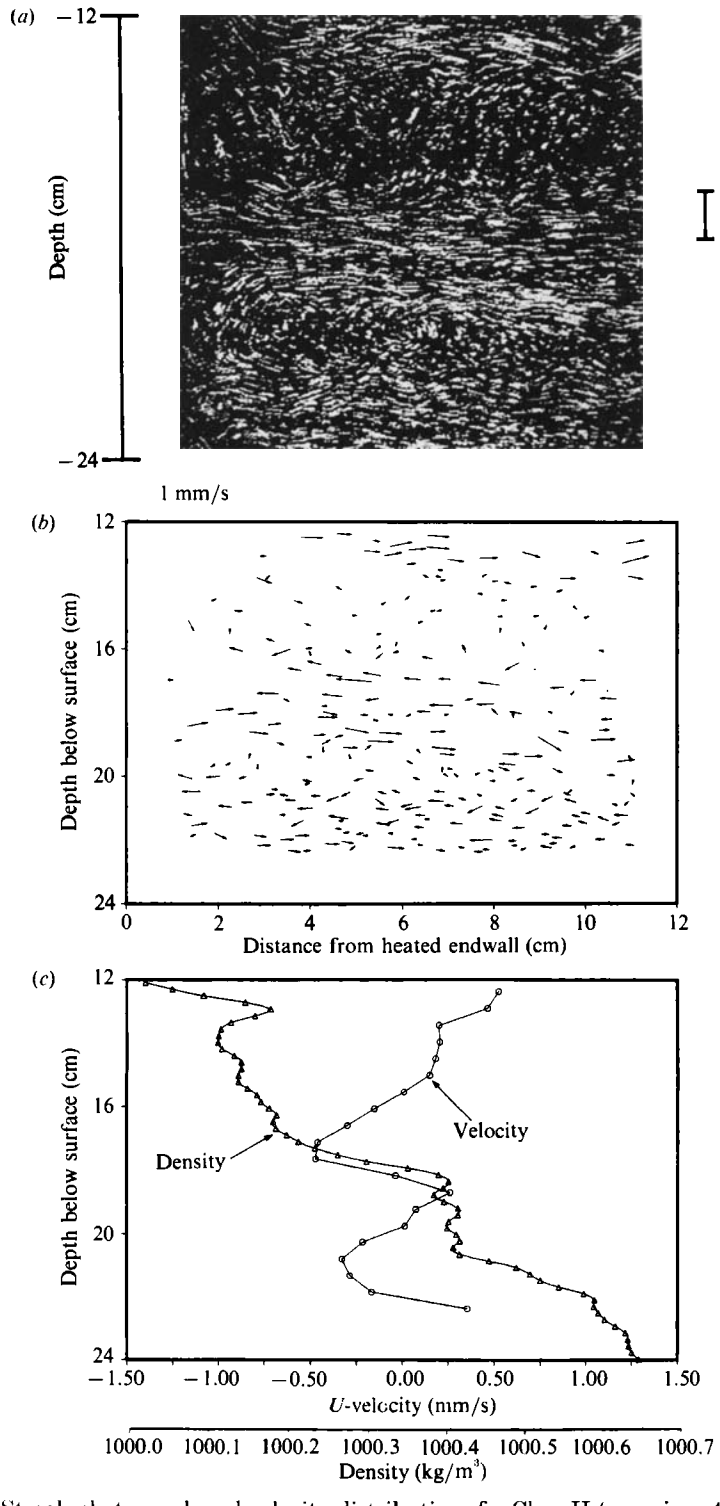

FIGURE 22. Streak photograph and velocity distributions for Class II (experiment II-3): (*a*) particle streak image generated over 8 s time period at $t = 100$ min, (*b*) two-dimensional velocity field obtained from streak image, (*c*) depthwise velocity and density profile 5.8 cm from heated endwall. Velocity profile is generated by interpolating from the vector field in (*b*).

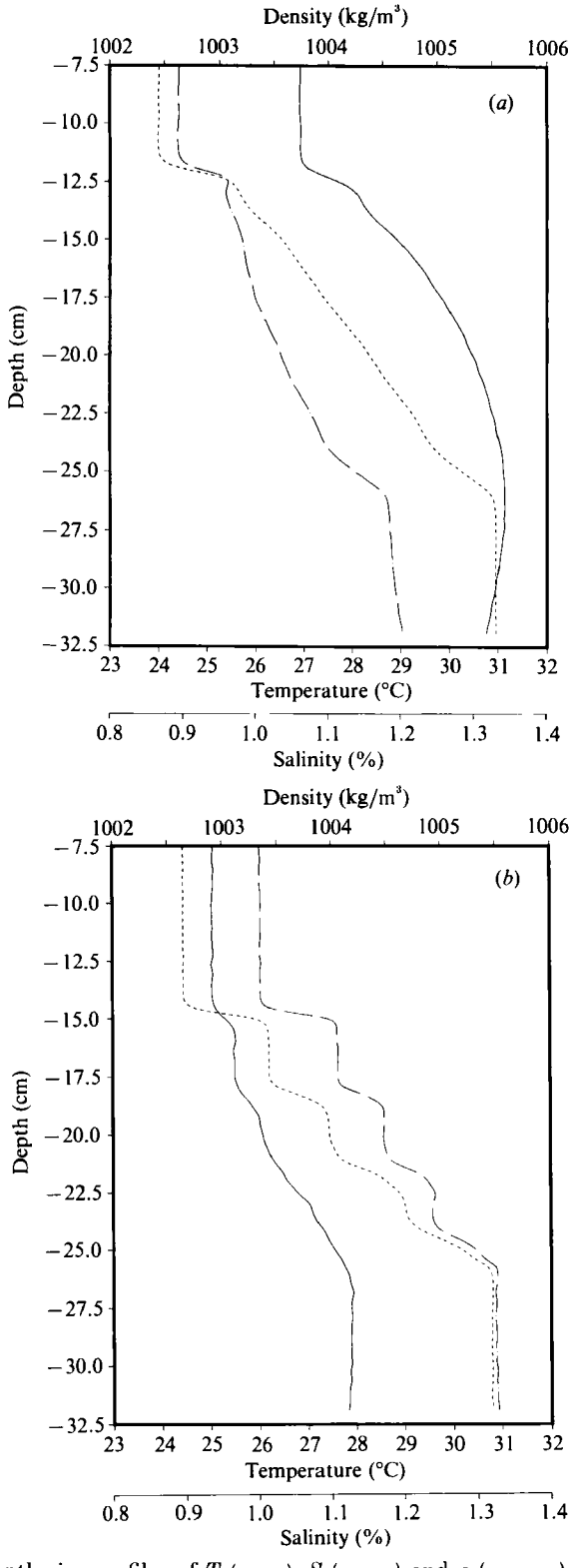

FIGURE 23. Depthwise profiles of T (——), S (– – – –) and ρ (—·—·) from experiment III-2, 3680 mm from the heated endwall: (*a*) $t = 93$ min, (*b*) $t = 793$ min.

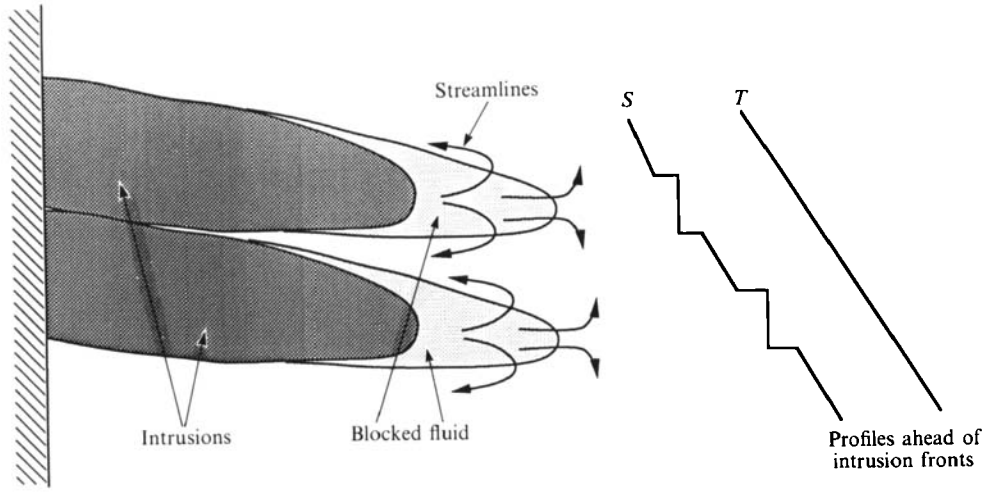

FIGURE 24. Schematic of blocking effect ahead of intrusions.

like signature, the intrusions have advanced to this point in spite of removal of the endwall heat flux 600 min earlier. Note that the steps in the temperature distribution of figure 23(*b*) are not nearly as well defined as those in the salinity, an indication that the intrusions have 'run down' and are no longer convectively active. Although the processes governing continued propagation of the intrusions have yet to be conclusively identified, one possible mechanism is discussed below.

Turner (1973) and Browand & Winant (1972) have described the effects of blocking ahead of an obstacle in a stratified flow. A similar blocking mechanism could also modify the flow field ahead of the intrusions. Figure 24 illustrates this process schematically. Owing to the presence of the far endwall, blocked fluid ahead of the intrusions is forced either upward or downward, producing corresponding disturbances in the vertical profiles ahead of the intrusion fronts. Because of its low diffusivity, salinity that is perturbed by the blocking effect tends to diffuse very slowly in the vertical direction. The heat diffuses very quickly, and thus the temperature profile remains effectively unchanged. This blocking mechanism can modify the vertical profiles ahead of the intrusions such that the local value of R_ρ is reduced in the upper region of each intrusion and is increased in the lower region.

Data supporting such modifications are presented in the series of profiles in figure 25. These profiles were taken during experiment II-3, 300 mm from the heated endwall at the times shown. At $t = 63$ min, both the salinity and temperature profiles have been modified slightly by the blocking mechanism. The difference in rate of diffusivity between temperature and salinity is apparent at $t = 110$ min, at which time several distinct convective regions are clearly visible in the salinity profile. The temperature profile, however, is still relatively smooth in comparison. By $t =$ 172 min, the intrusions are well defined in both profiles. Owing to the differences in magnitude between the coefficients of expansion α and β, the variations in the temperature profile at $t = 63$ min have an insignificant effect on the density and the local value of R_ρ. The variations in salinity, however, can substantially modify the local stability conditions. It is possible, if a critical value of R_ρ exists, that this modification could reduce the R_ρ below the critical value ahead of the intrusion. The intrusion could then continue to grow indefinitely, independently of the conditions that first set it in motion.

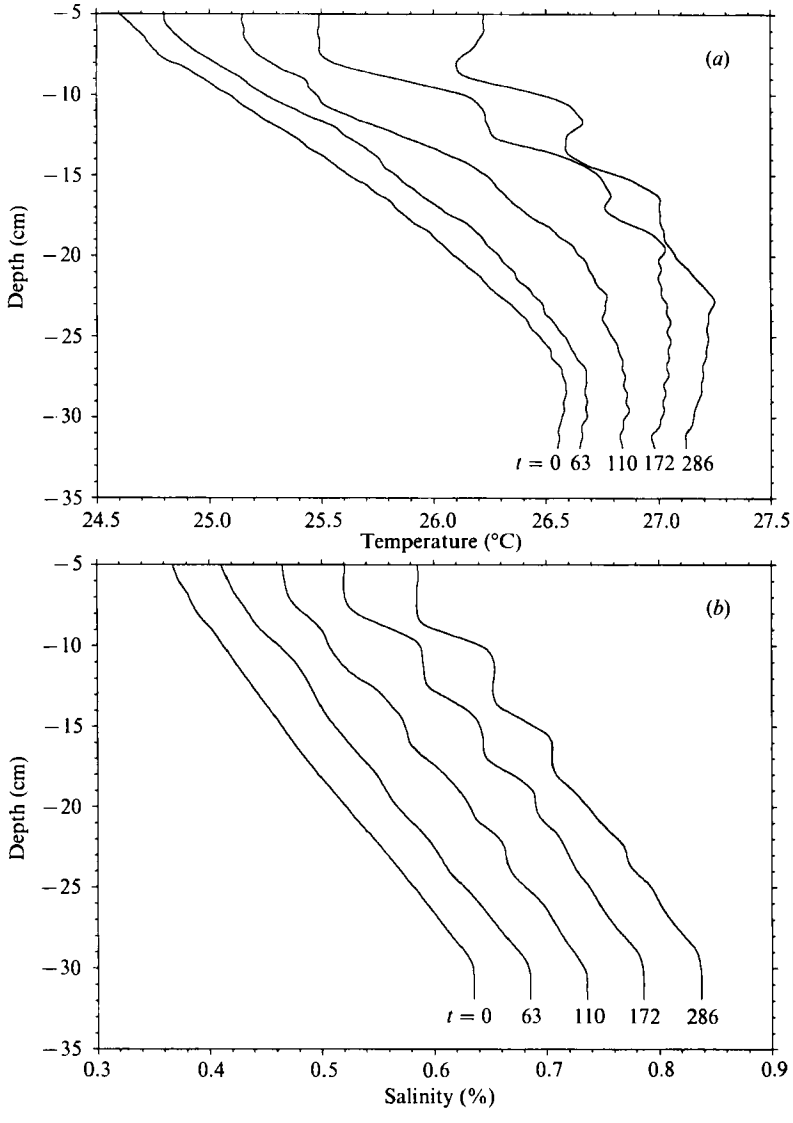

FIGURE 25. Series of profiles 300 mm from the heated endwall for experiment II-3. Times shown are in minutes. (*a*) Temperature (each profile offset by 0.2 °C), (*b*) salinity (each profile offset by 0.05‰).

5.4. *Summary and conclusions*

In summary, application of a uniform lateral heat flux to a linearly stratified heat/salt system has revealed some interesting intrusion dynamics and a much greater range of processes than previously observed with only single-component stratifications. Initially, the endwall heating causes the fluid to rise near the wall. Owing to the double-diffusive nature of the stratification, the fluid is forced out away from the wall producing a series of convective cells over the entire depth of the stratified region. For relatively high rates of heating ($R_1 > 5$), the results of a scaling analysis indicate that the initial size of these convective cells, h, is a function of both the endwall heat flux and the ambient stratification, as observed in the experiments.

However, the boundary-layer assumptions used to derive this scaling break down as $R_1 \to 1$, and thus the results are no longer valid for lower heating rates. An alternative scaling is not readily apparent for this case, although as $R_1 \to 1, h \to \delta$ indicating that the vertical and horizontal lengthscales are similar under the lower heating conditions.

As the initial convective roll cells grow into larger convective intrusions, a wide range of dynamic behaviour develops, depending upon the initial values of the stability parameters R_ρ and R_1. Consequently, the intrusions have been classified into three distinct classes based upon these stability parameters. Class I encompasses intrusions which develop under conditions of high gravitational and lateral stability (high R_ρ and low R_1) and which are very similar in appearance and behaviour to those observed for single-component stratifications. In contrast to Class I, however, the destabilizing component (temperature) in the vertical density gradient becomes much more significant in Classes II and III. Flows in these classes occur under less stable conditions (both gravitationally and laterally) and are characterized by larger-scale motions in terms of interfacial shear velocities, propagation velocities, intrusion thickness, and internal convective and mixing behaviour.

The internal structure of the intrusions, while varying in scale, is very similar in all three classes. Each intrusion is bounded above by a diffusive interface followed by a thin region of gravitational instability. Below this is a convective region dominated by salt fingering near the heated endwall, and characterized by zones of recirculation further from the endwall. Another diffusive interface then separates each intrusion from its neighbour below. While the fingering motions were first observed from flow visualization, T–S diagrams have been used to identify regions where fingering is likely to occur, based on local stability conditions. Analysis of the T–S diagrams in each class indicates that fingering occurs near the heated wall in all three classes and is an important component of the near-wall dynamics. In addition, results from the numerical simulation of a Class I flow provide supplemental information regarding the initial development of the intrusions which cannot be observed in the experiments. The intrusions first pass through an endwall convection stage at $O(10$ s) in which the fluid begins rising up the wall. At $O(20$ s), the double-diffusive nature of the system becomes apparent as a vertical flow reversal occurs. A 'fingering' period follows from 20–100 s at which time the flow becomes dominated by horizontal motions out along the top and in along the bottom of each intrusion.

In all three classes, the initial intrusions merge to form larger intrusions as they propagate away from the heated endwall. In Class I, the merging process appears to be controlled by motions external to the intrusions themselves, which are induced by horizontal shear waves propagating ahead of the intrusion fronts. Merging takes place as flows towards the heated endwall inhibit the outward propagation of 'weaker' intrusions, eventually forcing them back towards the wall where they are entrained by their 'stronger' neighbours. In Classes II and III, the merging occurs as a result of strong vertical (fingering) motions at the heated endwall within the intrusions themselves. These motions allow the interface between two adjacent intrusions to be eroded, resulting in a merging process that advances out from the endwall. In no case was merging found to be caused by shear instability or by an equalization of density across the length of the intrusion interface.

Following the merging of the intrusions to their preferred final thickness, they continue to propagate out away from the heated endwall. In Classes I and II, the propagation is controlled by the endwall heating. Once the endwall heat flux is removed, the process of the intrusions is halted and they recede back towards the

wall, eventually diffusing away. In Class III, however, the intrusions continue propagating even after the heat flux is removed. In order for this process to occur, the intrusions must be able to tap into the potential energy locked up in the destabilizing component (temperature) of the vertical density distribution. The suggested 'blocking' mechanism provides a means for the local value of R_ρ to be reduced below a critical stable condition. This condition defines the point at which the intrusions become self-perpetuating.

We greatly appreciate the assistance of Fred Heyler while conducting the experiments, Jonathan Harris for his help in developing the image processing software, and Stephen Monismith for his many useful suggestions regarding the content of this paper. In addition, the journal referees offered many valuable comments for which we are most grateful. This work is supported by the Department of Energy under grant DE-FG03-87ER13757. The numerical computations were performed at the NSF Supercomputer Centre in San Diego.

REFERENCES

BROWAND, F. K. & WINANT, C. D. 1972 Blocking ahead of a cylinder moving in a stratified fluid. *Geophys. Fluid Dyn.* **4**, 29–53.

CHEN, C. F. 1975 Double-diffusive convection in an inclined slot. *J. Fluid Mech.* **72**, 721–729.

CHEN, C. F., BRIGGS, D. G. & WIRTZ, R. A. 1971 Stability of thermal convection in a salinity gradient due to lateral heating. *Intl J. Heat Mass Transfer* **14**, 57–65.

CHEN, C. F., PALIWAL, R. C. & WONG, S. B. 1976 Cellular convection in a density-stratified fluid: effect of inclination of the heated wall. *Proc. 1976 Heat Transfer & Fluid Mech. Inst.*, pp. 18–32. Stanford University Press.

HEAD, M. J. 1983 The use of miniature four-electrode conductivity probes for high resolution measurement of turbulent density or temperature variations in salt-stratified water flows. Ph.D thesis, University of California, San Diego.

HUPPERT, H. E. & TURNER, J. S. 1980 Ice blocks melting into a salinity gradient. *J. Fluid Mech.* **100**, 367–384.

JEEVERAJ, C. G. & IMBERGER, J. 1991 Experimental study of double-diffusive instability in sidewall heating. *J. Fluid Mech.* **222**, 565–586.

KELLEY, D. 1984 Effective diffusivities within oceanic thermohaline staircases. *J. Geophys. Res.* **89**, 10484–10488.

LINDEN, P. F. 1976 The formation and destruction of fine-structure by double diffusive process. *Deep-Sea Res.* **23**, 895–908.

LINDEN, P. F. & WEBER, J. E. 1977 The formation of layers in a double-diffusive system with a sloping boundary. *J. Fluid Mech.* **81**, 757–773.

MAXWORTHY, T. 1987 The nonlinear growth of a gravitationally unstable interface in a Hele–Shaw cell. *J. Fluid Mech.* **177**, 207–232.

MENDENHALL, C. E. & MASON, M. 1923 The stratified subsidence of fine particles. *Proc. US Natl Acad. Sci.* **9**, 199–202.

NARUSAWA, U. & SUZUKAWA, Y. 1981 Experimental study of double-diffusive cellular convection due to a uniform lateral heat flux. *J. Fluid Mech.* **113**, 387–405.

OSBORN, T. R. 1988 Signatures of doubly diffusive convection and turbulence in an intrusive regime. *J. Phys. Oceanogr.* **18**, 146–155.

OSTER, G. 1965 Density gradients. *Sci. Am.* **212**, 70–76.

PATANKAR, S. V. 1980 *Numerical Heat Transfer and Fluid Flow.* Hemisphere. 197 pp.

PERNG, C. Y. & STREET, R. L. 1989 Three dimensional unsteady flow simulation: alternative strategies for volume averaged calculation. *Intl J. Numer. Meth. Fluids*, **9**, 341–362.

POSMENTIER, E. S. & HOUGHTON, R. W. 1978 Fine structure instabilities induced by double diffusion in the shelf/slope water front. *J. Geophys. Res.* **83**, 5135–5138.

RIGNOT, E. & SPEDDING, G. 1988 *'Spline Thin Shell' interpolation scheme. USCAE* 143. Dept. of Aerospace Engineering, Univ. of Southern California, Los Angeles.

ROBERTS, G. O. 1970 Computational meshes for boundary layer problems. In *Proc. 2nd Intl Conf. on Numerical Methods in Fluid Dynamics*. Lecture Notes in Physics, vol. 8 (ed. M. Holt), pp. 171–177. Springer.

RUDDICK, B. R. & SHIRTCLIFFE, T. G. L. 1979 Data for double diffusers: physical properties of aqueous salt–sugar solutions. *Deep-Sea Res.* **26A**, 775–787.

SCHLADOW, S. G. 1990 Oscillatory motion in a side heated cavity. *J. Fluid Mech.* **213**, 589–610.

SCHLADOW, S. G., PATTERSON, J. C. & STREET, R. L. 1989 Transient flow in a side-heated cavity at high Rayleigh number: a numerical study. *J. Fluid Mech.* **200**, 121–148.

SUZUKAWA, Y. & NARUSAWA, U. 1982 Structure of growing double-diffusive convection cells. *Trans. ASME* C: *J. Heat Transfer* **104**, 248–254.

TANNY, J. & TSINOBER, A. B. 1988 The dynamics and structure of double-diffusive layers in sidewall-heating experiments. *J. Fluid Mech.* **196**, 135–156.

THORPE, S. A., HUTT, P. K. & SOULSBY, R. 1969 The effect of horizontal gradients on thermohaline convection. *J. Fluid Mech.* **38**, 375–400.

TURNER, J. S. 1973 *Buoyancy Effects in Fluids*. Cambridge University Press.

TURNER, J. S. 1985 Multi-component convection. *Ann. Rev. Fluid Mech.* **17**, 11–44.

TURNER, J. S. & CHEN, C. F. 1974 Two-dimensional effects in double diffusive convection. *J. Fluid Mech.* **63**, 577–592.